Marine and Petroleum Geology 139 (2022) 105603

Contents lists available at ScienceDirect

Marine and Petroleum Geology

journal homepage: www.elsevier.com/locate/marpetgeo

Quantitative diagenesis: Methods for studying the evolution of the physical properties of tight carbonate reservoir rocks

F. Rashid [a], D. Hussein [b], P.W.J. Glover [c,*], P. Lorinczi [c], J.A. Lawrence [d]

[a] Kurdistan Institution for Strategic Studies and Scientific Research, Sulaimani, Kurdistan region of, Iraq
[b] Department of Geology, University of Sulaimani, Sulaimani, Kurdistan region of, Iraq
[c] School of Earth and Environment, University of Leeds, UK
[d] Department of Civil and Environmental Engineering, Imperial College London, UK

ARTICLE INFO

Keywords:
Cementation exponent
Diagenesis
Connectedness
Permeability
Tortuosity
Dolomitisation
Petrodiagenetic pathways

ABSTRACT

Conventionally, diagenesis has been studied by making qualitative morphological observations which have been organised into complex classification schemes. Petrophysics, with its many quantitative measurements, now gives us the ability to quantify the effects of the type, degree and timing of complex diagenetic process. The aim of this paper is to examine how different diagenetic processes affect the petrophysical properties of carbonate rocks and to develop quantitative methodologies to describe the results of diagenetic processes. A large number of petrophysical measurements have been made on a suite of 172 core plugs to provide a test data set. Diagenetic modification of the primary depositional fabric was observed in a wide range of measured petrophysical parameters, and that porosity and pore connectedness exert dominant control on all of the electrical and hydraulic rock parameters. This observation has been used to propose a new theoretical framework linking the effect of diagenetic process to petrophysical measureables. Cementation exponent was found to increase with permeability and pore size, especially in recrystallized rocks, and is explained by smaller porosity samples having a better connected pore network. Electrical connectedness was also found to correlate extremely well with hydraulic permeability, showing that these phenomena are linked closely in tight carbonate reservoir rocks. A method for calculating pre- and post-dolomitisation porosity and the degree of dolomitisation from the measured petrophysical and compositional data has also been developed and tested. All electrical and hydraulic properties are related to pore type, allowing cementation exponent to be obtained from optical microscopy/SEM studies or NMR measurements, providing a new approach to estimating cementation exponent in carbonate rocks. This paper also provides a powerful new approach allowing petrophysical changes associated with the type, degree and timing of different diagenetic processes to be tracked quantitatively using a method we have called 'petrodiagenetic pathways'.

1. Introduction

It is estimated that approximately half of all known global oil reserves occur in carbonate rocks. Furthermore, carbonate reservoirs provide nearly half of current hydrocarbon oil and gas production (Ramakrishnan et al., 2001; Akbar et al., 2008; Barros-Galvis, 2018). Carbonates are the dominant reservoir type in the Middle East (Hollis, 2011; Al-Qayim and Rashid, 2012; Al-Qayim and Othman, 2015; Hollis et al., 2017; Jafarian et al., 2017; Adam et al., 2018; Aldega et al., 2018; Bigi et al., 2018) and this region contains nearly 15% of the world hydrocarbon reserves (Normi and Standen, 1997).

The characterization of carbonate rocks in both conventional and tight reservoirs is complicated by a range of different diagenetic processes, which have modified the pore microstructure. These processes include compaction, dissolution, precipitation, dolomitisation, stylolitisation, fracturing and cementation (Anselmetti and Eberli, 1993, 1997; Anselmetti et al., 1997; Hussein et al., 2017; Rashid et al., 2017). Each diagenetic process occurs to different degrees, producing different morphological changes to the rock microstructure. Different diagenetic processes can occur recurrently, consecutively or penecontemporaneously, and often a diagenetic process occurring in one part of the rock formation is different and even dependent on another occurring in some proximal or distal part of the same or an associated formation. For example, mineral-rich fluids caused by the diagenetic process of stress

* Corresponding author. School of Earth and Environment, University of Leeds, Woodhouse Lane, LS2 9JT, UK.
E-mail addresses: fraidoon.rashid@kissr.edu.krd (F. Rashid), p.w.j.glover@leeds.ac.uk (P.W.J. Glover).

https://doi.org/10.1016/j.marpetgeo.2022.105603
Received 30 September 2021; Received in revised form 14 February 2022; Accepted 20 February 2022
Available online 28 February 2022

dissolution can be reprecipitated locally, which occurs during stylolitisation. The degree, style and timing of different diagenetic process are also inter-dependent. For example, dolomitisation produces a formation which is more likely to fracture (e.g., Liu et al., 2021) and the fractured rock mass is then both prone to compaction and to the influx of fluids which may result in further dissolution or precipitation, depending on the concentration of the fluid. The complexity and inter-related nature of diagenetic processes (Hollis et al., 2010) have resulted in their study conventionally being focussed on qualitative morphological observations which have been organised into complex classification schemes (e.g., Choquette and Pray, 1970; Lucia, 1995; Mohammed Sajed et al., 2021; Mohammed Sajed and Glover, 2020).

The range of parameters and measurements available to the modern petrophysicist now makes monitoring of the physical properties of rocks, and the evolution of reservoir quality, possible. This has started to allow the development of concepts that help describe the diagenetic processes, or at least their effects (Mohammed Sajed et al., 2021). Consequently, the study of diagenetic process and their effect on reservoir quality has begun to be able to be studied more quantitatively.

Important physical properties include (i) total, effective and potential porosities (Mohammed Sajed et al., 2021; Schofield et al., 2018), (ii) the η value (Rashid et al., 2015b), (iii) cementation exponent and formation factor (Glover, 2015), and (iv) chemical composition of the matrix. These parameters are often available, particularly from routine and special core analysis. All of these parameters are modified by diagenetic processes because all of them depend on the microstructure which the diagenetic processes alter.

The size distributions of pore-throats, pores and grain sizes are critical parameters, which contain a wealth of information about the morphology of the pore space, including its size and its likely interconnectivity. These distributions are often simplified to provide a single-valued 'characteristic' pore-throat, pore and grain size, which is that size that has the same effect as the assembly of the whole of each distribution. These parameters describe how the matrix is diminished by diagenetic processes such as dissolution, comminution and gouge formation, or augmented by (re)precipitation and cementation, and how the pore spaces react to those changes. For clastic rocks the characteristic pore-throat, pore and grain sizes can be calculated from each other (Glover and Walker, 2009), and used to predict the permeability through the RGPZ equation (Glover et al., 2006). This is possible because there is a physical relationship between grain size and pore size for clastic rocks that arises from their clastic origin. This relationship is not present for carbonate rocks due to the operation of diagenetic processes, particularly dissolution, reprecipitation, cementation and recrystallisation. However, permeability can still be predicted using a modified version of the RGPZ model that uses the empirical η parameter (Rashid et al., 2015b) and also allows pore-throat, pore and grain size calculations, the equation for which is developed later in this work.

The triad of linked properties composing porosity φ, cementation exponent m, and formation factor $F = \varphi^{-m}$, are also extremely important (Glover, 2015). This is because they describe both how the storage of fluids in the rock changes with diagenesis and how connected the pore spaces are, thus influencing the permeability. Since diagenetic processes perturb both porosity and the connectedness (Glover, 2009) of pore spaces, these parameters are indispensable for tracking microstructural changes caused by diagenesis.

The cementation exponent (sometimes called factor or index) was first introduced by Archie (1942), and was given this name because, at that time, he thought that it was related to the process of cementation. We now know that this is not the case, and that the cementation factor or exponent is actually related to the electrical connectedness of the pores in the rock (Glover, 2015). Consequently, cementation is only one of many primary and diagenetic processes which may affect the cementation exponent. There now exists a set of formal differential equations that define the meaning of the cementation exponent (Glover, 2009) and which provide a physical meaning of the cementation exponent as the rate of change of the electrical connectedness of a rock with respect to changes in its porosity and connectivity (Glover, 2010).

Archie's combined first and second laws can be used to calculate the hydrocarbon saturation of a rock (Archie, 1942; Glover, 2015). Archie's combined first and second laws for a single conducting phase can be written as

$$S_o = 1 - \left(\frac{R_w \varphi^{-m}}{R_t}\right)^{1/n}, \quad (1)$$

where; S_o is the fractional saturation of hydrocarbons in the rock, R_w is the resistivity of the aqueous pore fluid (Ω.m), R_t is the bulk resistivity of the partially hydrocarbon-saturated rock (Ω.m) (Glover, 2015), φ is the porosity (fractional), n is the saturation exponent (no units) (Glover, 2017), and m is the cementation exponent (no units) (Glover, 2016; Wang et al., 2014; Carpenter et al., 2009; Chen et al., 2009). If two or more conducting phases are present the 2-phase (Glover et al., 2000) or n-phase (Glover, 2010) versions of Archie's law should be used. A small change in the cementation exponent can lead to a much larger change in the calculated rock resistivity because it exponentiates the porosity. For example, if m changes from 2 to 2.2 while the other parameters are kept constant at typical reservoir values ($R_w = 0.5\ \Omega$ m, $R_t = 500\ \Omega$ m, $\varphi = 0.1$ (10%), and $n = 2$), the hydrocarbon saturation increases by 25.9% (from 0.316 to 0.398) which is likely to represent tens of millions of dollars in 'lost' or unexpected and unplanned revenue. Consequently, it is extremely important to know the value of m accurately (Borai, 1987), especially in rocks which have had their pore connectivity altered by diagenetic processes closing or widening pore throats.

In this paper we measure the petrophysical characteristics of tight carbonate reservoir rocks, including the magnitude of cementation factor, and we examine the major controls on the main physical properties of the rocks with reference to primary depositional processes and subsequent diagenetic history.

The aim of this research is to understand better the link between diagenetic processes, concomitant rock microstructural changes and the physical properties discussed previously in order to start to quantify the effect of diagenetic processes on reservoir quality. Analytical methods for calculating the post- and pre-diagenesis porosities have been developed, together with methods for tracking post- and pre-diagenesis permeabilities and monitoring the effect of diagenesis using a new method which we call petrodiagenetic pathways.

2. Sampling and methodology

Core plugs were taken from the Cretaceous Kometan formation which contains tight carbonate reservoir rocks occurring throughout the Kirkuk embayment oil fields of the Zagros folded and thrust belts of north-eastern Iraq (Fig. 1). The samples were collected from 5 drilled wells, one from each of the Taq Taq, Kirkuk, Khabaz, Bai Hassan, and Jambur oil fields (Al-Qayim and Rashid, 2012; Al-Qayim and Othman, 2012).

A total of 172 core plugs were extracted from the original core samples for laboratory measurements in this study. The core plugs were nominally 1.5″ in diameter and 2" long. The plugs were cleaned using the Soxhlet method and oven dried at 100 °C for 24 h. The plugs were drilled parallel to the bedding plane. Samples were not taken both parallel and perpendicular to bedding, as previous work on these samples has shown that the vertical and horizontal permeabilities in these samples are similar (Rashid et al., 2017). Consequently, it is an assumption of this work that the observed isotropy in the hydraulic connectivity of the rocks infers an isotropy in the electrical connectivity of the rocks.

A wide range of petrophysical laboratory tests were conducted (Table 1). All 172 core plugs were subjected to helium porosimetry and pulse decay Klinkenberg-corrected permeability analysis. A smaller number of core plugs were selected for further measurements based on

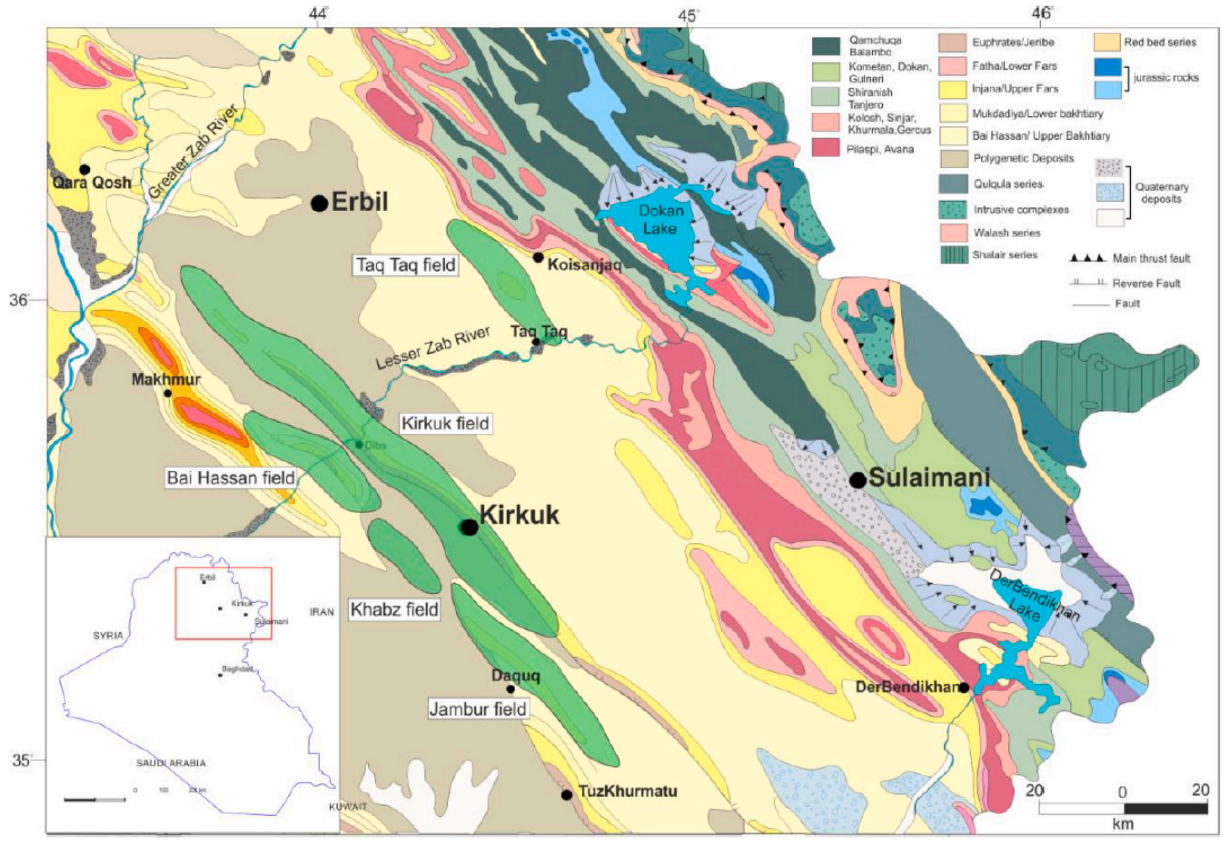

Fig. 1. Geological map of the Kurdistan region and north-eastern Iraq showing the selected fields of the study area, modified from (Rashid et al., 2020; Sissakian et al., 2000).

Table 1
The range of tests carried out in this work.

Methodology and/or parameter	Number of samples	Uncertainty	Comments
Pulse decay permeametry	172	±5%	Using the methodology described in Jones (1997)
Helium porosimetry	172	±0.1%	Using the apparatus and protocols at the Wolfson Multiphase Flow Laboratory at the University of Leeds, UK
X-ray diffractometry	8	±2%	Using a PW1050 XRD apparatus
SEM compositional analysis	22	±2.5%	Using the built-in EDAX system
SEM pore analysis	22	±1%	Quantitative analysis carried out with ImageJ ver. 1.53e
Mercury injection capillary pressure, porosity, pore throat, pore size and grain size distributions	23	±3%	Using a Micromeritics Autopore IV 9250 apparatus. Pore sizes and pore throat sizes were calculated using the methods of Glover and Walker (2009) and Glover and Déry (2010)
Electrical resistivity, formation factor and cementation exponent	19	±2%	Made using an impedance spectrometer operating at 1 kHz and analysed according to conventions found in the review Glover (2015)
Nuclear magnetic resonance (NMR) spectroscopy	23	±4%	Using a MARAN 2 apparatus

the observed porosity-permeability relationships.

Mineral composition was determined using an X-ray diffractometer (PW1050 XRD technique). A total of 8 samples were measured based on their physical appearance, lithofacies and porosity-permeability relationships. The samples were prepared by crushing to an average grain size of 8 μm diameter using a McCrone micronising mill. The benefit of this approach was to provide a material with a more uniform grain size.

A helium gas expansion pycnometer was used to measure the connected porosity on all 172 core plug samples. The porosity value φ was calculated from the grain volume and bulk volume to within ±0.1% using the apparatus and protocols at the Wolfson Multiphase Flow Laboratory at the University of Leeds, UK.

As it was known that the samples would have a low permeability, the permeability was measured using a PDP 200 helium pulse-decay permeameter. This apparatus measures permeability by monitoring the decay of gas pressures as a fixed mass of gas passes into a sample (Jones, 1997). The permeability measurement was repeated four times for each sample with different pore pressures to allow the Klinkenberg-corrected permeability for each sample to be calculated (Tiab and Donaldson, 2004). This is very important because the Klinkenberg effect is particularly pronounced in tight rocks with small pore sizes and porosities. The permeability was measured using a confining pressure of 800 psi.

Subsets of 22 samples with polished surfaces were selected for image analysis using high-resolution HRFE-SEM techniques. The samples were selected based on results obtained from the porosity and permeability relationships and sample lithofacies. Images were taken at magnifications of ×10 and × 20. The surfaces of the samples were polished, cleaned and then coated with gold to provide a conductive surface layer for each sample. Such SEM images are widely used to identify pore types (Wang et al., 2014). In this study, the images were analysed using ImageJ image analysis software and implementing a segmentation technique to provide a 2D sample porosity. The average pore diameter of

each sample was measured using the Feret's diameter approach.

High pressure mercury injection capillary pressure (MICP) tests were carried out using a Micromeritics Autopore IV 9250 apparatus to obtain curves for 23 samples. The samples were cut (1 × 1 × 2 cm) and oven dried at 100 °C. Mercury was injected into the sample using 62 pressure stages from 1 to 60,000 psig (0.00689–413.68 MPa); the pressures were correlated logarithmically to pore-throat size using the Washburn equation. A pore-throat size correlated to the threshold pressure point on the capillary pressure curve can be considered as an effective pore-throat size in tight carbonate rocks in this study (Rashid et al., 2015b, 2017; Rashid et al., 2015b). The characteristic pore size and grain size distributions were calculated from the pore-throat size distributions using the methods in Glover and Déry (2010) and in Glover and Walker (2009), respectively.

Nuclear magnetic resonance (NMR) spectroscopy measurements were performed on fully brine-saturated plug samples. The NMR measurements were conducted on a MARAN 2 bench top spectrometer at 25 °C and at atmospheric pressure, providing the logarithmic T_2 distribution from 0.01 ms to 1000 ms.

A subset of 19 core plugs was selected for electrical measurements in order to calculate the cementation exponent. The chosen core plugs were saturated with brine of 25,000 ppm NaCl using a vacuum technique followed by soaking for 2 days at 25 °C and 1000 psig (6.89 MPa) pressure to ensure complete saturation. The saturated samples were then encased in an electrically isolated core holder with non-polarising electrodes. An electric current (AC frequency, $f = 1 \pm 0.001$ kHz, voltage, $V = 1 \pm 0.01$ V) was applied to the core plug until a steady-state was achieved, at which point the frequency, voltage and current were all logged. The saturated core plug resistance was converted to resistivity R_o using the core plug dimensions. The apparatus was previously calibrated against a set of standard resistances (1 ± 0.01 Ω, 10 ± 0.1 Ω and 20 ± 0.2 Ω). The electrical properties of the rock (formation factor F, connectedness G, cementation exponent m, and tortuosity, τ_e) were calculated in accordance with the methods set out in Glover (2015). This process involves the measurement of the resistivity of the pore fluid R_w, which was carried out using a resistivity meter. The formation factor F and connectedness G were calculated according to the definitions $F \equiv R_o/R_w$ and $G \equiv R_w/R_o$, respectively. The cementation exponent was then calculated using

$$m = -\ln(F)/\ln(\varphi)\,, \tag{2}$$

where φ is the core plug's fractional porosity, and the electrical tortuosity was calculated by using

$$\tau_e = \varphi^{1-m}\,. \tag{3}$$

It should be noted that the use of a fixed frequency of 1 kHz and an in-phase current and voltage method has advantages over a full impedance spectroscopy approach in that it is much easier, faster and cheaper. However, it assumes that electrode polarization does not affect the measurements and that the electric current is in-phase with the electric potential at that frequency; this is usually a justifiable assumption in most reservoir rocks (see review in Glover, 2015).

3. Experimental results

3.1. Mineralogy

X-Ray diffraction analysis shows that the majority of the samples are composed mostly of calcite as expected (Table 2), with a minimum calcium carbonate ($CaCO_3$) content of 90.87%. Two samples were very clean, both containing 98.55% of calcium carbonate. Two samples contained dolomite ranging from 4.50% to 7.41%. All samples contain small fractions of quartz minerals ranging between 0.66% and 4.23%. Illite-smectite dominated the clay fractions, which were always less than 3% of the total composition in all samples, while chlorite and kaolinite were absent. No pyrite or mica were identified in the samples.

Table 2
X-Ray diffraction results for the eight samples studied.

Sample	Quartz (%)	Calcite (%)	Dolomite (%)	Illite-Smectite (%)
K1	4.23	95.77	0.00	0.00
K4	3.39	95.34	0.00	1.27
K7	1.64	95.87	0.00	2.49
K9	1.45	98.55	0.00	0.00
K10	1.45	98.55	0.00	0.00
K11	1.72	90.87	7.41	0.00
K13	0.66	94.84	4.50	0.00
K18	3.01	96.99	0.00	0.00

3.2. Pore type and size

The size of pores of each of the samples was classified by dividing them into three types using SEM data and the Rashid et al. (2017) classification, which is a modification of the Choquette and Pray (1970) scheme. The classes were (i) nano-intercrystalline pores, which were defined as pores with pore sizes less than 1 μm, (ii) micro-intercrystalline pores, which were defined as pores with pore sizes between 1 μm and 10 μm, and (iii) meso-intragranular and moldic pores, which were defined as pores with pore sizes greater than 10 μm.

The dataset studied in this work was composed of samples representing all three classes (as shown in Table 3). Nano-intercrystalline pores were recorded with pore sizes between 0.009 μm and 0.90 μm, with an arithmetic mean value of 0.17 μm, micro-intercrystalline pore sizes between 1.01 μm and 8.95 μm, with an arithmetic mean value of 2.43 μm, and meso-intragranular and moldic pores with pore sizes between 10.36 μm and 130.39 μm, and an arithmetic mean value of 48.43 μm. Fig. 2 shows SEM micrographs of typical pore spaces corresponding to each of the classes, while Fig. 3 shows the distributions of pore sizes from SEM image analysis using ImageJ and colour-coded according to the implemented classification.

The grain radius is related to the pore radius in clastic rocks by the relationship (Glover and Walker, 2009)

$$\frac{r_{grain}}{r_{pore}} = \frac{mF}{\sqrt{3}}. \tag{4}$$

However, this equation is based on relationships which are not valid for carbonate rocks and which underlie the RGPZ permeability prediction equation (Glover et al., 2006). Rashid et al. (2015b) modified the RGPZ equation to make it applicable to carbonates by introducing a scaling term η which allows the ratio of the grain to pore radius to be much larger, accounting for the growth of grains and closure of pore spaces by recrystallisation. This also makes the RGPZ equation empirical because the value of η is not calculable and must be measured. Introducing this same term into Equation (3) leads to

$$\frac{r_{grain}}{r_{pore}} = \frac{m\eta F}{\sqrt{3}}, \tag{5}$$

which would be capable of producing a grain size distribution from the pore size distribution presented earlier, but will only be accurate if η is constrained by some independent measure of grain radius such as image analysis.

3.3. Pore-throat size

Mercury injection capillary pressure measurements provide a method for the measurement of pore-throat size as well as a measure of connected porosity and a drainage capillary pressure curve. In this study the measured pore-throat diameter ranged from 0.009 μm to 0.5 μm (as shown in Fig. 4), with the summary data also given in Table 3. It is remarkable that the predominant sizes of pore throats do not vary

Table 3
Pore system types classified in accordance with the Rashid et al. (2017)/Choquette and Pray (1970) of the measured samples together with their experimental ranges.

Pore type	Measured range of pore diameters (μm)	Arithmetic mean of measured pore diameters (μm)	Modal value of measured pore diameters (μm)	Measured range of pore throat diameters (nm)	Modal value of measured pore throat diameters (nm)
Nano-intercrystalline	0.009–0.90	0.17	0.187	3.0–86	72
Micro-intercrystalline	1.01–8.95	2.43	1.662	120–900	126
Meso-intragranular and moldic	10.36–130.39	48.43	14.35	50–900	201

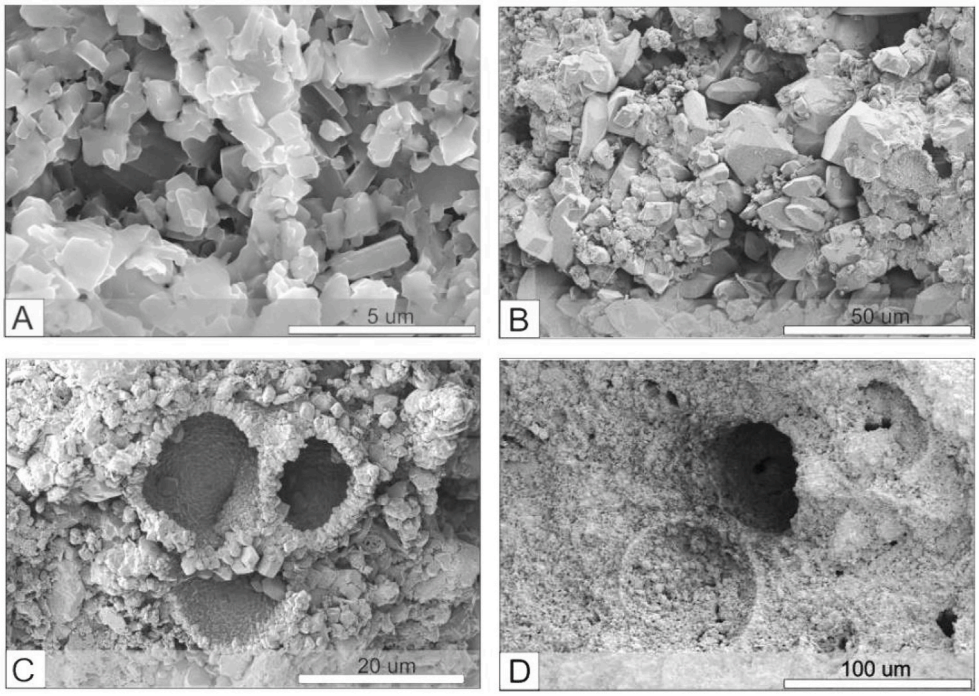

Fig. 2. SEM micrography of selected samples; A: Nano-intercrystalline pore type between calcite crystals, B: Micro-intercrystalline pore type between calcite crystals, C: Meso-intragranular pores that preserved as isolated pores, D: Meso-intragranular and moldic pores that interconnected through micro pore-throats.

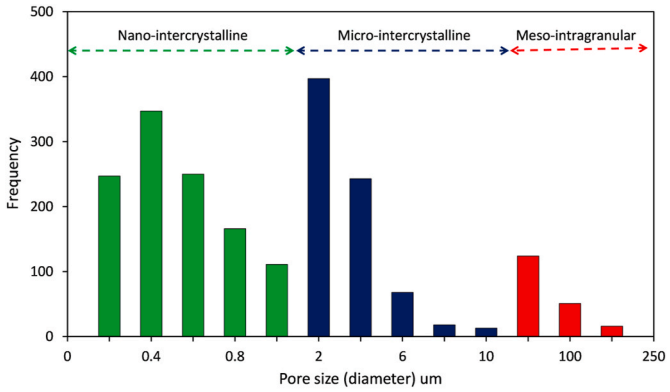

Fig. 3. Pores size distribution achieved from SEM images. Nano-intercrystalline pores, size <1.0 μm, micro-intercrystalline pores, size from 1.0 μm to 10 μm, and meso-intragranular and moldic pores, size >10 μm.

greatly between any of these very different pore microstructures. The nano-intercrystalline pores have pore-throat sizes ranging from 0.003 μm to 0.086 μm with an arithmetic mean of 0.072 μm achieved from the threshold pressure point. The micro-intercrystalline pores exhibit pore-throat sizes ranging from 0.012 μm to 0.90 μm with an arithmetic mean of 0.5 μm, while the meso-intergranular and moldic pores have pore-throat sizes ranging from 0.050 μm to 0.90 μm with an arithmetic mean of 0.660 μm.

Consequently, and counter-intuitively, the pore throat size may not be the main control on the fluid flow and electrical properties of each of the pore types. The meso-intergranular pore type has been split between those not containing large moldic pore spaces (Fig. 4C) and those which do contain them (Fig. 4D). This is to examine whether pore-throats leading to larger moldic pores are larger than those between the smaller pores which make up the majority of the pore space in the rock. The similarity in the modal values in parts C and D of Fig. 4, together with the almost non-existence of a high pore-throat tail in Fig. 4D shows that moldic pores are no better connected (i.e., have pore throats which are no larger) than the other pores in the rock, and hence it would be expected that their presence would not improve the permeability of the rock; an observation that has been made previously (Rashid et al., 2015a).

3.4. Porosity and permeability

The measured helium porosity and Klinkenberg-corrected helium permeability relationship is presented in Fig. 5. The nanoporous core plugs show porosities in the approximate range 0.05–0.08, considerably smaller than the porosities exhibited by the microporous samples (approximately 0.125–0.26) and mesoporous/moldic samples (approximately 0.19–0.29). While there is a clear distinction between the nanoporous samples and the other two pore types, the microporous and mesoporous/moldic pore types exhibit a considerable degree of overlap in their porosity and permeability values. This is because the

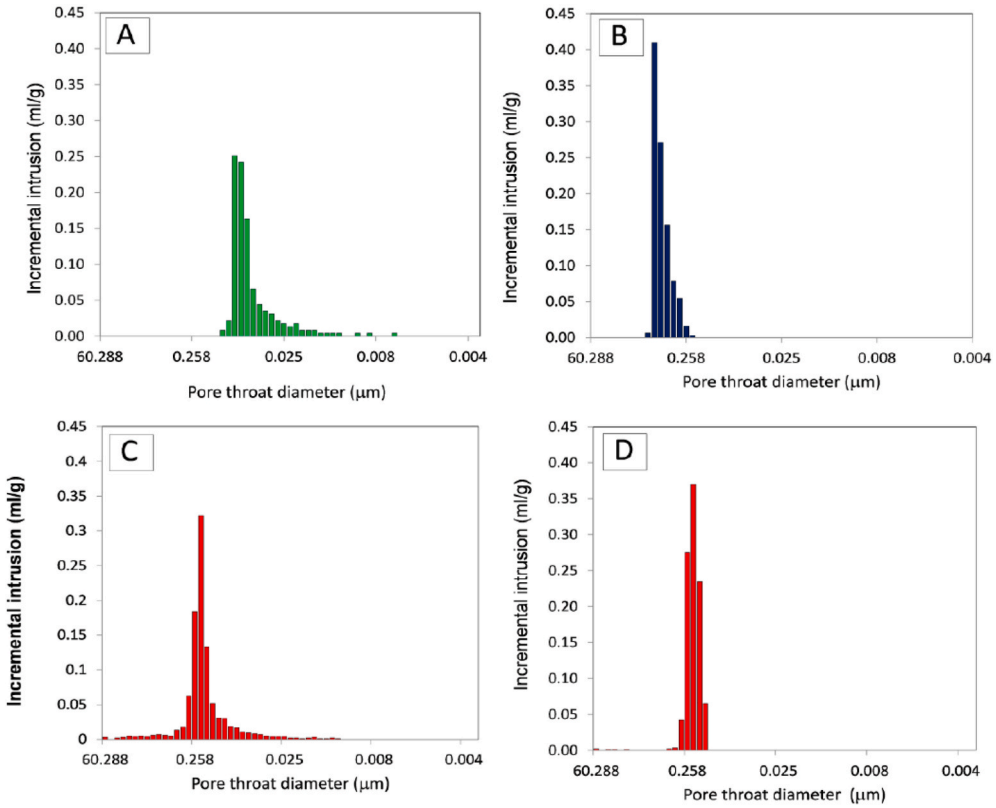

Fig. 4. Pore-throat size distributions from mercury injection capillary pressure measurements of typical sample for each pore type: (A) nano-intercrystalline pores, (B) micro-intercrystalline pores, (C) meso-intragranular pores, and (D) meso-intragranular with moldic pores.

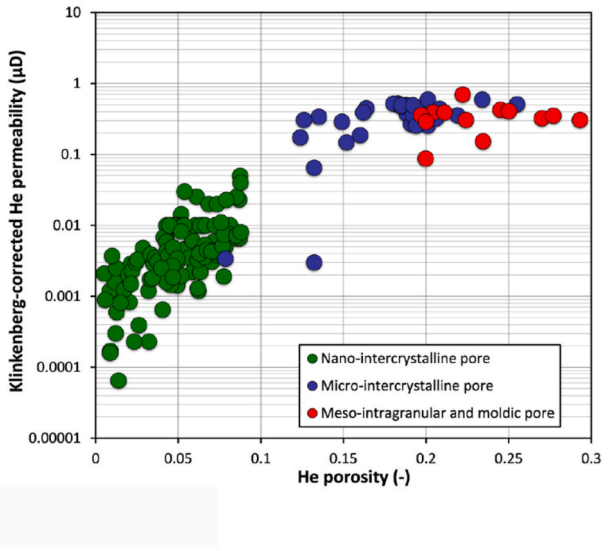

Fig. 5. Poroperm plot of the measured Klinkenberg-corrected permeability as function of helium porosity of the plug samples from the Kometan formation in five oil fields and one licensed block in the Kirkuk embayment of the Zagros basin, (n = 150).

categorisation is based on pore type rather than porosity and permeability. While the nanoporous pore type has distinctly different porosities and permeabilities from the other two, the microporous and mesoporous/moldic pore types contain some rocks which express similar porosities and permeabilities.

The permeability data range differs over five orders of magnitude from 0.65 ± 0.08 μD to 700 ± 0.08 μD. The nanoporous core plugs show permeabilities less than 60 μD, while microporous and mesoporous/moldic samples exhibit permeabilities in the range 0.123–0.70 mD. There is little distinction in the permeabilities of the microporous and mesoporous samples despite the higher porosity of the latter. This is because the extra porosity is in the form of isolated large moldic pores that do not contribute to increasing the hydraulic connectivity of the sample, and hence do not increase the permeability significantly.

It is not the purpose of this paper to discuss the poroperm relationships in the Kometan formation further as this has already been covered in previous papers which show that the heterogeneous relationships between porosity and permeability in this formation reflect the fact that petrophysical properties in carbonate rocks are controlled by rock texture and diagenetic modifications (Rashid et al., 2015a, 2015b, 2017). However, porosity and permeability are closely connected to cementation exponent theoretically, making the presentation of this data essential in any discussion about cementation exponents.

3.5. Electrical properties

The electrical properties of the selected core plugs are shown in Table 4, Fig. 6 and Fig. 7. There is a clear separation in electrical behaviour between the three pore types, which is exhibited in all of the electrical parameters. Plotting the formation factor as a function of porosity on a log-log scale allows straight contour lines to be drawn for a range of cementation exponents as in Fig. 6 (where the cementation exponent varies from m = 1.2 to m = 3.8).

It can be seen that the three pore types are clearly separated in the figure, with the smaller porosity, small pore and pore-throat size pores exhibiting cementation exponents between m = 1.2 and m=2.0, while the medium porosity, medium pore and pore-throat size micro-intercrystalline rocks have 2 < m < 2.4, and the large vuggy meso-intergranular rocks have 3.0 < m < 3.8). Since low cementation exponents are associated with better connected pore networks, this trend in

Table 4
Electrical properties of measured core plugs.

Core plug	Pore type	Helium porosity φ (±0.05%)	Formation factor F (±0.05%)	Electrical connectedness G ($\times 10^{-3}$±0.05%)	Cementation exponent m (±0.05%)	Electrical tortuosity τ_e (±0.05%)	Electrical connectivity χ_e (±0.05%)	Klinkenberg-corrected permeability k (mD ±0.05%)
K1	Nano-intercrystalline	0.03697	382.7	2.61	1.80	14.15	0.07	0.00092
K2		0.0498	346.4	2.89	1.95	17.25	0.06	0.00090
K3		0.01208	798.3	1.25	1.51	9.64	0.10	0.00018
K4		0.06606	181.9	5.50	1.91	12.01	0.08	0.00869
K5		0.0249	317.0	3.15	1.56	7.89	0.13	0.00240
K6		0.0495	208.3	4.80	1.78	10.31	0.10	0.00680
K7		0.02148	325.9	3.07	1.51	7.00	0.14	0.00290
K8		0.01242	316.8	3.16	1.31	3.93	0.25	0.00250
K9		0.02612	607.8	1.65	1.76	15.85	0.06	0.00041
K10		0.05	136.7	7.31	1.64	6.84	0.15	0.00630
K11	Micro-intercrystalline	0.1321	126.7	7.89	2.39	16.74	0.06	0.00300
K12		0.15174	63.0	15.9	2.20	9.55	0.10	0.16340
K13		0.1829	55.6	18.0	2.37	10.17	0.10	0.19580
K14		0.217	23.5	42.5	2.07	5.10	0.20	0.62640
K15		0.07855	178.8	5.59	2.04	14.04	0.07	0.00340
K16		0.1881	36.0	27.8	2.14	6.76	0.15	0.28280
K17	Meso-Intragranular and moldic	0.1996	194.7	5.14	3.27	38.86	0.03	0.01750
K18		0.2344	89.5	11.2	3.10	20.97	0.05	0.15290
K19		0.2769	98.9	10.1	3.58	27.37	0.04	0.10710

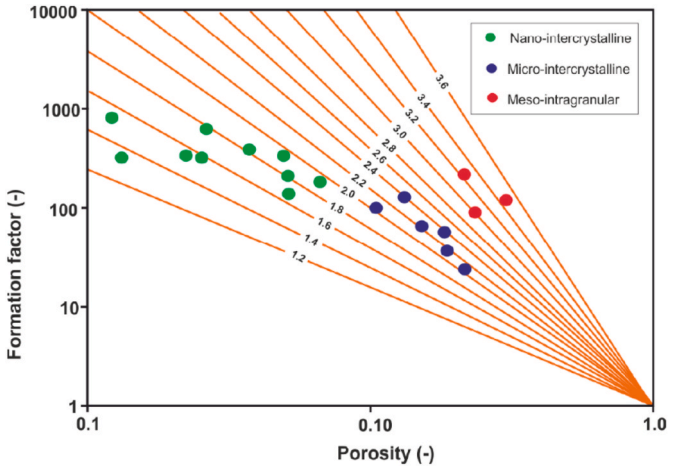

Fig. 6. Calculated formation resistivity factor (log scale) as function of measured helium porosity (log scale) used for determination of cementation exponent factor (Schlumberger, 2009).

cementation exponents runs contrary to expectations. We would expect that carbonate rocks with smaller pores and pore-throats would present less-well-connected pore networks, whereas these results show that the reverse is true, at least for water saturated rocks where the electrical flow is used as a measure of pore connectivity. The good connectivity exhibited by nano-intercrystalline rocks does not aid fluid flow because the pores and pore throats are so small that the capillary pressure that needs to be overcome for fluid flow to occur is too high. Hence, there is a highly electrically connected pore network which does not support fluid flow.

We would expect fluid flow to be more constrained by small pores and pore-throats resulting from interactions between the fluid and the rock matrix that are formalised by wettability and capillary pressure considerations. Hence, a reduced porosity called the 'potential' porosity has been defined (Schofield et al., 2018) where it is recognised that fluids cannot pass through pores and pore-throats less than a given size because they represent a capillary pressure barrier that the normal pressures associated with fluid flow in reservoirs (naturally developed or arising from artificial pumping) cannot overcome. The threshold value of pore/pore-throat diameter is usually taken as 50 μm for oils and 5 μm for gases.

Since both of these thresholds are larger than the characteristic pore sizes and pore-throat sizes encountered in the rocks in this work, it may be argued that the observed apparent higher connectivities for the nano-intercrystalline rocks, which the lower cementation exponents would infer, is irrelevant to fluid flow because oils and gases cannot overcome the capillary pressures required to enable them to make use of this fine, highly connected network. Although, it may also be noted that the difficulty in accessing such pores might leave them unsaturated during experimentation and hence not be accounted for in the subsequent measurement of the R_o that is used to calculate formation factor and cementation exponent.

The behaviour of the meso-intragranular and moldic pore type is anomalous. The high formation factors (low connectednesses) of these samples are unexpected and may arise from access of larger pores being restricted by very small pore throats. This behaviour is possible, especially in moldic pores where the access to pore throats may be occluded with undissolved material when the body of the bioclasts have been fully dissolved to form the mould, or when the outer layer of the bioclast is less soluble than its body.

A summary of the electrical properties of samples as a function of their helium porosity and classified into nano-crystalline, micro-crystalline and meso-intercrystalline/moldic pores is given in Fig. 7.

The nano-crystalline pore types have large formation factors (>100) and low porosities (Fig. 7a). These high formation factors are controlled by the very low porosities of these samples (i.e., <7%). However, Fig. 6 shows how much higher the formation factors of these rocks would be (1000–10,000) if their cementation exponents were equal to or larger than that for a typical clastic rock (m = 2.0). It is the high pore connectivities (low tortuosities, <20; Fig. 7d) associated with their low cementation exponents (<2.0; Fig. 7c) that keep the formation factors lower than 1000. By contrast, Fig. 7 also shows that the microporous core plugs exhibit much lower formation factors (<100 for all but 1 sample; Fig. 7a), and associated higher connectednesses (>0.01 for all but 1 sample; Fig. 7b). These values are, once again, controlled by the porosity of the samples, which are significantly greater (13.2%–21.7%) than for the nanoporous core plugs.

The cementation exponents for the microporous samples fall in the range $2 < m < 2.5$ (Fig. 6), indicating that the pore networks of the microporous samples are more anfractuous than the nanoporous samples, however the broadly similar derived electrical tortuosities (<20; Fig. 7d) suggest that the electrical tortuosity is also being controlled by

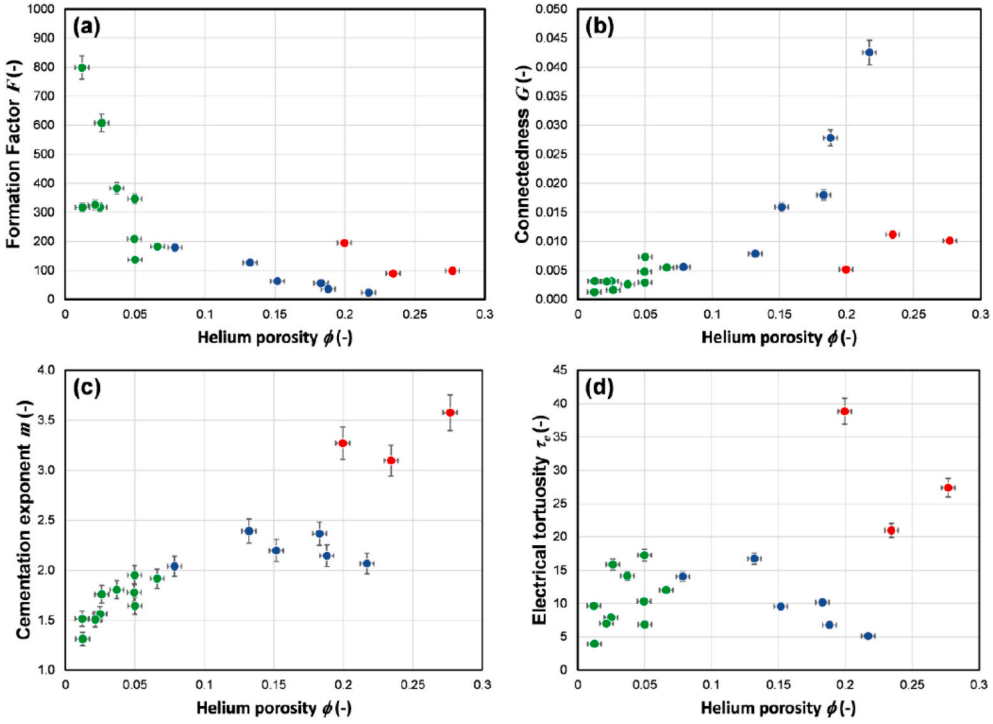

Fig. 7. The electrical properties of selected samples of the Kometan formation measured in this work as a function of helium (connected) porosity. (a) Formation factor, (b) connectedness, (c) cementation exponent, and (d) electrical tortuosity. In each case samples are classified according to pore type, with nano-crystalline pores in green, micro-crystalline pores in dark blue and meso-intercrystalline/moldic pores in red. (For interpretation of the references to colour in this figure legend, the reader is referred to the Web version of this article.)

porosity. The direct link between cementation exponent and tortuosity is given in Equation (3) above (Glover, 2015).

The mesoporous/moldic samples exhibit a third type of behaviour. These samples have the highest porosities (>20%; Figs. 6 and 7), but the high porosities do not result in formation factors (and connectednesses) correspondingly lower (and higher) than the microporous samples (Fig. 7a and b, respectively). Clearly, not only porosity controls these parameters. The cementation exponents for these samples are high (>3; Fig. 7c), as are the electrical tortuosities (>20; Fig. 7d). In these samples the additional porosity compared to the other two pore types is in the form of large moldic pores, which do not improve the overall electrical flow in the rock. Consequently, their porosity does not contribute effectively to electrical transport and the cementation exponent and electrical tortuosity consequently increases.

3.6. Electrical connectedness and permeability

It would be expected that hydraulic and electrical transport would behave similarly because both are controlled by how well the pore network is connected. In the case of hydraulic transport, the network must be connected by pore-throats large enough for fluids to flow through them, i.e., with capillary pressures less than the fluid pressure driving the fluid flow. In the case of electrical transport, the connectivity includes any electrically open pathways including those containing aqueous bulk fluids, electrical double layers and conductive solids (Höltzel and Tallarek, 2007).

The cementation exponent is often considered to be a measure of how well the pore network is connected, with lower cementation exponents related to pore networks which are more directly connected. Consequently, one might expect higher permeabilities to be associated with lower cementation exponents. The top plot in Fig. 8 shows cementation exponent as a function of Klinkenberg-corrected permeability. The plot shows unexpected behaviour. Although there is a large degree of scatter, there is a weak tendency for cementation exponent to increase with permeability. Clearly, for these tight carbonate rocks, the microporous and nanoporous samples have higher permeabilities due to their higher porosities, and despite exhibiting a lower connectivity as indicated by their slightly higher cementation exponents. Another method needs to be employed to examine the effect of the electrical connectedness and its relationship with permeability.

The bottom part of Fig. 8 shows a plot of electrical connectedness as a function of Klinkenberg-corrected permeability, which shows a remarkable correlation given that the electrical and hydraulic measurements are entirely independent. The correlation holds true for all pore types and over 4 orders of magnitude of permeability. This figure shows clearly that the connectedness G is the electrical analogue of hydraulic permeability. The electrical connectedness is the product of the electrical connectivity χ (which is the inverse of the electrical tortuosity) and porosity, according to $G = \chi\varphi$ (Glover, 2010).

3.7. Cementation exponent, pore size and NMR measurements

In this study the pores were subdivided into three pore types based upon pore size; nano-intercrystalline, micro-intercrystalline and meso-intercrystalline/moldic pore types. The measured data shows that the cementation exponent is also related to pore size (here the characteristic pore diameter was calculated by image analysis using ImageJ) (Fig. 9). Samples with larger pore sizes are associated with larger cementation exponents for these tight carbonate rocks. As with the relationship between cementation exponent and permeability, this association is counterintuitive and indicates that the prediction of cementation exponent in tight carbonates is not a simple process. Given the sensitivity of water saturation and reserves calculations to cementation exponent, our recommendation is that there is the potential to predict cementation exponent in the absence of electrical wireline logs by using NMR, providing the relationship is calibrated with laboratory measurements on core plugs.

The longitudinal relaxation time distributions (T_2) obtained from the NMR analysis can be calibrated to provide a set of pore size distributions using the results of studies of different reservoir rocks with large pore diameters having longer T_2 values (Westphal et al., 2005; Hussein et al., 2018). We have carried out this procedure and find a derived pore size distribution which clearly distinguishes between the three different main classes of pore texture. Fig. 10 shows all of the NMR T_2 spectra for

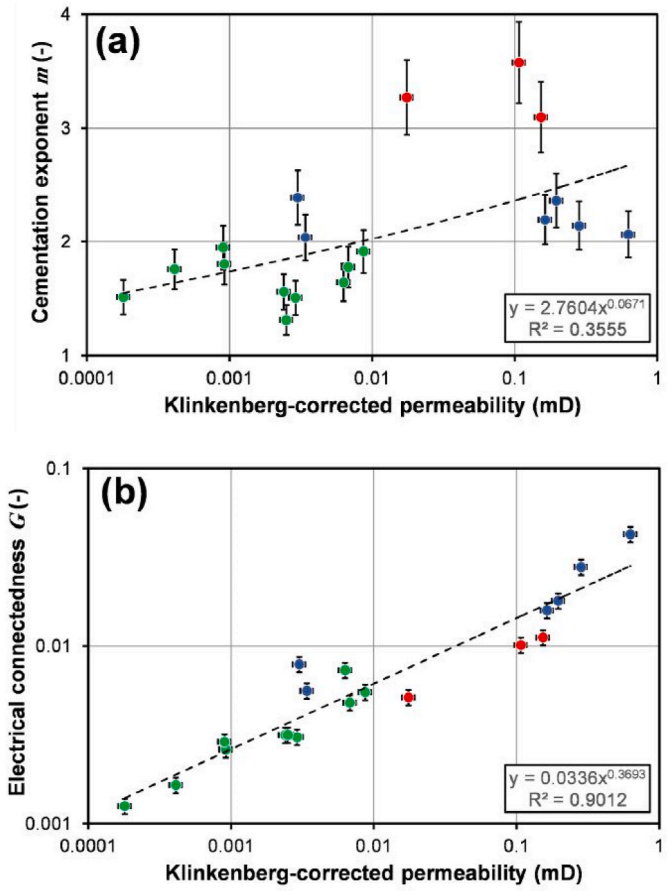

Fig. 8. Plot of (a) the cementation exponent, and (b) the electrical connectedness G (Glover, 2015), both as a function of Klinkenberg-corrected permeability, with the best fit power law and fitting parameters. In each case samples are classified according to pore type, with nanocrystalline pores in green, microcrystalline pores in dark blue and mesocrystalline/moldic pores in red. (For interpretation of the references to colour in this figure legend, the reader is referred to the Web version of this article.)

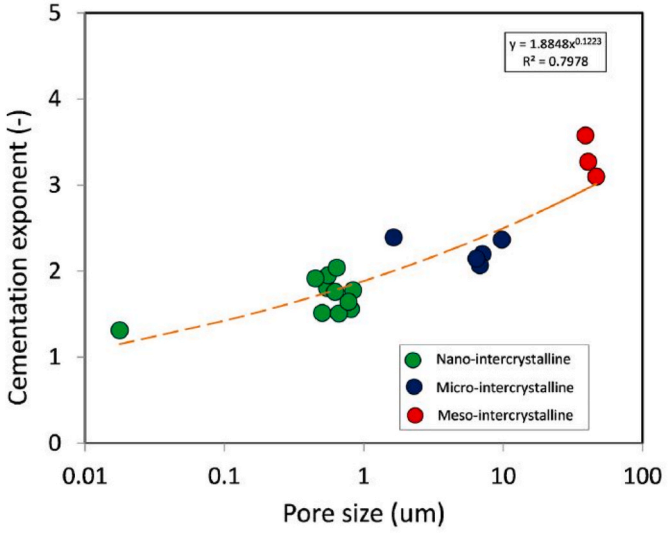

Fig. 9. The measured cementation exponent (m) as a function of the measured pore size achieved the SEM image analysis of the of all pore types.

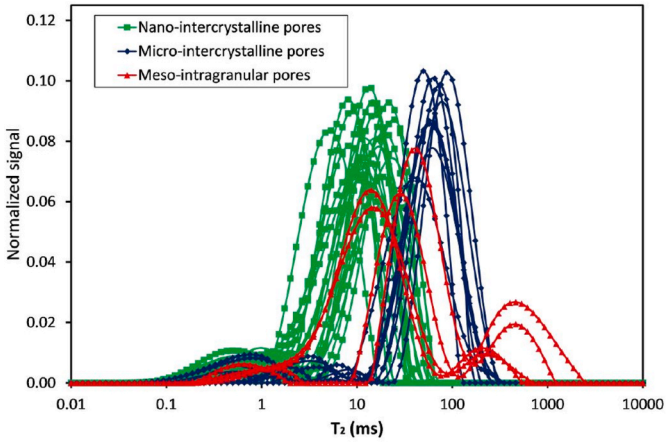

Fig. 10. T_2 distribution curves obtained from NMR spectrometry. Nano-intercrystalline pores have T_2 spectra <100 ms, micro-intercrystalline pores have T_2 spectra <200 ms, and meso-intragranular and moldic pores have T_2 spectra >200 ms.

each of the 23 samples tested. The samples with recognised nano-intercrystalline pores all provide short relaxation times, lower than 100 ms. By contrast, those samples showing micro-intercrystalline pores have clearly higher value of T_2, between 100 ms and 200 ms. The meso-intergranular pore samples, of which four were tested, exhibit the highest magnitude of T_2, which is greater than 200 ms and reaches to 1000 ms.

It has been recognised that cementation exponent can be approximated if the pore type is known from optical or SEM microscopy studies. The nano-intercrystalline pore types with a pore size 0.009–0.90 μm generally have a cementation exponent smaller than 2, as shown in Fig. 7 and Table 3. By contrast, the cementation exponent values of the micro-intercrystalline pore type with a pore size between 1.01 μm and 8.95 μm are located between 2 and 3. The highest values of the cementation exponent, greater than 3, coincide with pore sizes greater than 10 μm, and are associated with meso-intragranular and moldic pores. This recognised association of cementation exponent with grain size provides a new approach to estimating cementation exponent in carbonate rocks without the need for expensive special core analysis measurements.

4. Diagenesis and rock physical properties

In this section we seek to discuss the links between diagenetic processes and microstructural parameters describing the rock morphology, together with phase fractions and phase connectednesses as key parameters upon which all measureable petrophysical properties depend. We start with a brief theoretical framework, before discussing the links between diagenetic processes and phase fractions and connectednesses, then finish by examining quantitatively each of six diagenetic processes using data presented in this paper and that provided by the literature.

4.1. Theoretical framework

Conventionally two petrophysical parameters can be considered to describe most if not all aspects of the porous or fractured rock. These are the volume of a phase composing the rock and its connectedness (Cai et al., 2017; Glover, 2010). Fig. 11 shows these two parameters schematically. Each is shown as stacked multiple items to represent that the rock is composed of different phases, such as pore space and matrix. If more detail is required, the various fluid phases occupying the pore space and/or the different solid phases composing the matrix can be each considered as a separate phase.

There is a set of petrophysical properties which depend upon the

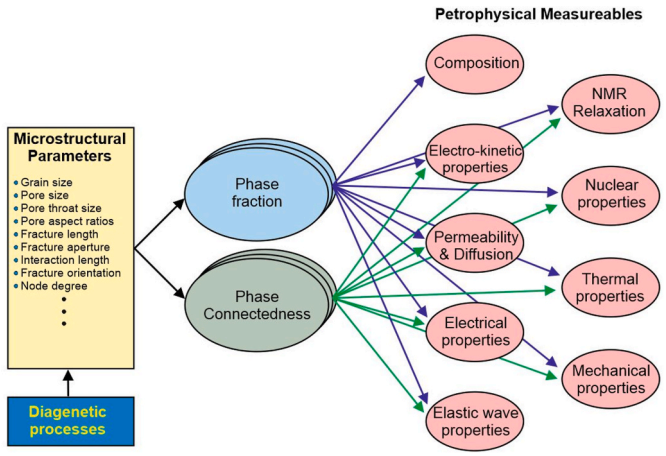

Fig. 11. Schematic representation of the relationships allowing diagenetic processes to alter the physical properties of rocks.

phase fractions and connectednesses that are shown to the right of Fig. 11. These properties, such as permeability, elastic wave and electrical properties will be more dependent on the fraction or connectivity of some phases compared to other phases. For example elastic wave properties depend more on the fraction and connectivity of the matrix than that of the pore space.

Likewise, there are microstructural parameters which together describe the microstructure of the rock and usually take the form of distributions. The microstructural parameters (Garum et al., 2021a; 2021b), which are shown on the left of Fig. 11, control the phase fractions and phase connectednesses. They include grain, pore and pore throat, fracture aperture, fracture length and fracture orientation distributions.

Diagenetic process act to alter the microstructural properties (Mohammed Sajed et al., 2021), and it is by modifying these that diagenesis changes the phase fractions and phase connectednesses and hence the physical properties of the rock.

It should be noted that although some physical properties are controlled by variations in the fraction and connectedness of some phases than others, the fractions and connectednesses of phases are not independent. Consider a simple 2-phase system composed of a matrix and pore space. If the phase fraction of the pore space (the porosity) increases the phase fraction of the matrix must decrease. Likewise, if the connectedness of the pore space increases (with or without a change in porosity), the increased connectedness of the pores will cut into and reduce the connectedness of the matrix. Hence, N phase fractions χ_i are connected by a law of conservation of volume

$$\sum_{i=1}^{N} \chi_i = 1 \tag{6}$$

and N phase connectednesses G_i are connected by a law of conservation of connectedness

$$\sum_{i=1}^{N} G_i = 1 \tag{7}$$

as described in Glover (2010) and Cai et al. (2017) for the electrical problem, and hypothesized to be general in this work.

Consider, for example, that the phase in question is the pore space. In this case the volume of the pore space is described by porosity and its connectedness is described by a set of connectivities which include its geometric, electrical or hydraulic connectivities. The geometric connectivity describes the morphological connectivity of pores, while the electrical and hydraulic connectivities describe how the geometric connectivity operates on the passage of a flow of charge or fluid mass, respectively.

If one was to take the rock matrix as the phase in question, the volume fractions of minerals and their connectednesses would control other parameters, such as elastic wave velocities and attenuations and heat flow properties. Once again microstructural parameters play a role in how connected one part of the matrix is to another, either facilitating or hindering the passage of elastic wave energy.

Diagenetic processes change the microstructural parameters that control the volume and connectednesses of all the phases of which rocks are composed, and hence affect all rock physical properties. In this work we seek to start to quantify the link between diagenetic process, the morphogenetic changes to the rock microstructure and the influence on the overall properties of the rock. This is clearly a huge undertaking, and so we will start by considering porosity, cementation exponent and permeability. Porosity is a measure of the volume of pore space in the rock, while cementation exponent and permeability are measures of the electrical and hydraulic connectednesses of the rock, respectively.

4.2. Diagenesis and porosity

Porosity is an important parameter. Not only does it control the space within the rock for storage of fluids (water, hydrocarbons and CO_2), it is related to the connectedness of the pore microstructure. It is an uncomfortable truth that without porosity there can be no pore pathway through the rock. This might seem a trivial observation, but it leads to the inextricable linking of porosity, formation factor and tortuosity that lies behind Archie's laws (see Glover (2015) for a review).

Porosity, whether as pores, fractures, molds or vugs, is commonly altered by diagenetic processes through the reworking of the rock's microstructural parameters. Since most petrophysical properties depend in some way upon porosity (Fig. 11), diagenetic process can modify all rock physical properties.

Take, for instance, the diagenetic process of precipitation. Precipitation in pores will reduce the size of the pore, and hence the porosity of the rock. The precipitation of a 1 μm layer of precipitate in a rock containing spherical pores of 20 μm diameter will reduce the porosity to 72.9% of its initial value, i.e., from 10%, say, to 7.29%. However, if these pores were connected by pore throats of 2 μm diameter, the same precipitation would block the pore throat, leading to a much greater effect on the connectedness of the pores. Consequently, we might expect that poroperm plots would show large changes in permeability for small changes in porosity concomitant upon diagenetic precipitation, such as we find in this work for the nano-intercrystalline pores in Fig. 5. The same argument applies in reverse for dissolution and especially for pressure dissolution.

It is difficult for some diagenetic processes to completely eliminate porosity because of its link with fluid flow. Precipitation requires the addition of material dissolved in pore fluids from which the pore-filling material can be formed. Consequently, progressive precipitation requires a connected porosity to be present. Likewise pores and pore pathways cannot be opened further by dissolution if the dissolving fluids do not have access to the pores through an existing transudatory pathway. In these cases the state of stress may result in compaction and other deformation that might exacerbate or protect the rock from further diagenetic change, but conversely, the inability of fluid to flow out of a pore space might strengthen the rock against the compacting influence.

4.3. Diagenesis and connectedness

The connectedness of a phase is defined as the phase fraction raised to an exponent (Glover, 2010). For the pore space, the phase fraction is the porosity and the exponent is the cementation exponent. Hence it is possible to say that the cementation exponent contains the information about how well the pores are connected.

Greater connectedness of pores is associated with smaller exponents. Consequently, for example, the (matrix) exponent for a well-indurated

rock will be closer to 0 than 1, indicating that there is extremely good connectedness between grains and resulting in, for example, higher elastic wave velocities, lower attenuation and improved thermal conduction. If we consider the pore space, a compact rock will have a more tortuous pore space with a (cementation) exponent that is larger than 2 and sometimes approaching 4 or 5. These high cementation exponent rocks, of which tight carbonates are a member, have consequently lower connectednesses which leads to lower absolute and relative permeabilities and electrical conductivities.

In this work the magnitude of the measured cementation exponent changes dramatically throughout the measured core plug samples. While there is a clear separation of cementation exponent values according to the pore type as discussed earlier, it is important that the factors controlling the size of the cementation exponent are understood in detail because small changes in cementation exponent can lead to large changes in estimated hydrocarbon reserves calculations.

Plotting formation factor against porosity on logarithmic scales (Fig. 7) shows clearly how the value of cementation exponent, which can be read from the figure parametrically, depends upon porosity and formation factor, and occupies separate fields in the φ - F space.

One of the goals of this paper is to examine the type, degree and timing of diagenetic processes which lead to the separation of cementation exponent (and other measured parameters) according to what have been conventionally classified as pore types, such that the cementation exponent for tight carbonate rocks can be related to diagenesis and hence better estimated.

The mineralogy of the rock is one possible factor. However, in this study all of the samples contain over 90% $CaCO_3$, and commonly over 95%. The remainder is made up of either (i) clay minerals, but never more than 2.49%, (ii) quartz, up to 4.23%, and (iii) dolomite up to 7.41%. Consequently, the test dataset does not contain sufficient variability in composition to properly test any inherent control that composition might have on cementation exponent or any of the other parameters measured in this work.

It is not possible to say that primary deposition has had little effect on cementation exponent for the data in this paper for two reasons. First, we have no direct evidence for microstructure of the rock prior to diagenesis. Second, the now lost primary depositional microstructure is likely to have influenced the diagenetic processes, and hence have had a 'relict' influence on the current cementation exponent (and other petrophysical properties). Previous studies of the Kometan formation (Rashid et al., 2015a, 2015b, 2017) have shown no evidence that the grain, pore and pore-throat size distributions associated with primary deposition have influenced the measured cementation exponent (or other parameters) because the microstructure of these tight carbonate rocks seems to have been very significantly remodelled by diagenetic processes. All of the tight carbonates measured in this work show signs of significant diagenesis, being highly cemented and compacted, often recrystallized, and occasionally dolomitized. Consequently, we assume that the primary depositional features of the rocks have not exerted a significant control on the cementation exponent. By contrast, all of the processes of diagenesis have the potential of significantly altering the cementation exponent.

4.4. Compaction

Compaction tends to affect the whole of a rock mass, reducing the porosity, pore size and, critically, reducing the pore-throat size to zero. This last effect leads to significant decreases in both hydraulic and electrical connectedness, which decreases permeability strongly, while also increasing electrical formation factor and decreasing electrical conductivity. By contrast, the cementation exponent only increases if a significant number of pathways for electrical conduction decreases. This effect can be seen in the data presented in this work. Considering the nano-intercrystalline pore type shown in Figs. 5 and 7 as the green data points, the small size of these pores and smaller pore throats would be thought to be closed easily by compaction. If we associate decreasing porosity with increasing compaction, the permeability decreases by almost 3 orders of magnitude as compaction increases and porosity decreases. However, all the electrical properties show different behaviour. Electrical connectedness (Fig. 7b) decreases with compaction as expected, indicating an overall less connected pore space, and hence lower conductivities. However, the cementation exponent (Fig. 7c) decreases with compaction indicating that pore throats are still open at least to the passage of electrical currents. The reason for the observed differences is that, upon compaction, pore throats are closed to such an extent that the capillary pressure that must be overcome is too high for fluid flow to occur, but the passage of electrical current is not impeded. Consequently, by making both hydraulic and electrical measurements of a rock, and comparing them, it is possible to recognise changes in the rock microstructure due to compaction.

4.5. Precipitation

Precipitation also reduces porosity and pore sizes, and can reduce the pore-throat size locally to zero resulting, it would be expected, in the same outcomes as occur for compaction. However, the pore throat blockages that occur due to precipitation are usually more localised than for compaction. The degree of precipitation depends upon the flow of mineral-rich fluid phases, and hence pore throats with larger initial apertures will undergo greater precipitation. Indeed, precipitation will slow down and stop as the pore throat is sealed. This self-limiting behaviour is likely to make the reduction of permeability less than in the case of compaction, but the difference between hydraulic flow and electrical transport discussed above can still operate.

4.6. Dissolution

By contrast with the cases described above, dissolution opens up and widens pore spaces, enhancing porosity and increasing pore sizes. In general dissolution may be pervasive, but rarely results in the opening-up of new pathways for hydraulic or electrical flow because its effects are usually restricted to slightly enhancing existing flow pathways (Gomez-Rivas et al., 2015). Indeed, existing flow is usually a prerequisite for dissolution in order that the dissolved material may be removed (Rashid et al., 2015a; 2017; Alsharhan and Sadd, 2000; Gomez-Rivas et al., 2015; Martín-Martín et al., 2013). Pressure solution, such as occurs in stylolite formation, is also unlikely to result in new flow pathways because compaction concomitant upon pressure solution immediately seals pathways (Heap et al., 2014) and the concentration of clays along the stylolite forms an effective flow barrier.

The local preferential dissolution of a mineral filling a fossil mould, for example, may increase the porosity of the rock significantly, yet the isolated nature of the new porosity has insignificant effect on the hydraulic or electrical flow through the pore network as a whole because the permeability is enhanced only locally (Westphal et al., 2005; Rashid et al., 2015a; Liu et al., 2018, 2019; Zhu et al., 2020).

Counterintuitively, dissolution can lead to higher electrical tortuosities and cementation exponents because the new porosity is not distributed effectively throughout the pore network where it can aid fluid and electrical flow, but resides in large and isolated pores and molds, where it plays no role in improving the connectedness of the pore network (Rashid et al., 2017). This may be recognised in the data in this paper, where cementation exponent (Fig. 7c) and electrical tortuosity (Fig. 7d) of the samples containing vugs (red symbols) are high compared to the same host rock without vugs (the blue symbols). The vugs increase the porosity of the rock, but reduce the electrical connectedness, and increase the cementation exponent and the tortuosity.

Consequently, precipitation tends to result in moderately lower permeabilities, higher formation factors and lower connectednesses, higher cementation exponents and electrical tortuosities but the

opposite process of dissolution leads to slightly higher permeability, slightly lower formation factors and lower connectednesses, together with higher cementation exponents and electrical tortuosities. This latter effect can be seen clearly in our data (Fig. 7) and qualitatively in thin-sections for the same samples reported previously (Rashid et al., 2015a, 2017), where the cementation exponent and electrical tortuosity of the mesoporous/moldic samples is high.

4.7. Recrystallisation

Extensive recrystallisation of a carbonate reservoir rock is generally associated with high temperatures in the presence of a mineral-rich fluid (Dix and Mullins, 1987; Lawrence, 1991; Mozley and Burns, 1993; Hesse et al., 2004). This process has the potential for completely remodelling the matrix structure and the pore network. Resulting pore networks are characterized by low porosities. Grain size may be larger or smaller than that of the primary fabric (Mohammed Sajed and Glover, 2020), but both pore sizes and pore-throat sizes are small, which leads to low permeabilities (Mohammed Sajed et al., 2021). Potential porosity (Luo and Machel, 1995) is also very small because the pores and pore-throats are often too small to allow fluid to flow at geologically reasonable fluid pressure differences (Serra, 1984). However, formation factors can be lower than one might expect with correspondingly higher connectednesses. This is because there are many interconnected grain boundary pathways pervading the rock, that though narrow are highly interconnected, reducing the rock's electrical tortuosity and cementation exponent. The same effect has been recognised in both Lochaline and Fontainebleau sandstones, where the process of quartz overgrowths reduced porosity, pore sizes and pore-throat sizes, but the cementation exponents became lower because the resulting multitude of thinner conduction pathways were more direct than was the case for the pore network of the primary depositional quartz sandstone without overgrowths (Walker and Glover, 2018). The data in this work shows evidence of the same processes occurring. The nano-intercrystalline samples represent recrystallized fabric with extremely small pores and pore-throats that are nevertheless highly connected. They present formation factors which are lower than would be expected (Fig. 7a) and corresponding higher connectednesses (Fig. 7b). Cementation exponents are lower than the other pore types (Fig. 7c), indicating low tortuosites (Fig. 7d), which arise from the improvement in the directness of flow across the rock by the myriad of thin pathways.

Hence recrystallisation, as a diagenetic process, may result in a rock with an improved connectedness, permeability and electrical conductivity even if its overall porosity remains low.

4.8. Dolomitisation

Dolomitisation causes widespread increases in porosity which enhances pore and pore-throat diameters, and consequently causes large increases in permeability, and electrical connectedness, with resulting diminution of cementation exponent and electrical tortuosity (Mohammed Sajed and Glover, 2020). The porosity enhancement occurs at depth and results in the mechanical equilibrium being perturbed. Consequently, dolomitisation often leads to subsequent compaction and faulting (Davies and Smith, 2006) giving rise to localized high porosity/high permeability hydrocarbon plays characterized by faults arranged in flower structures (Luczaj et al., 2006).

In an attempt to quantify the effect of different degrees of dolomitisation on porosity, we have developed an equation to calculate post-dolomitisation porosity from the pre-dolomitisation porosity, or *vice versa*. The porosity enhancement is due to the density differential between calcite $CaCO_3$ ($\rho_{LMST} = 2710$ kg/m^3) and dolomite $CaMg(CO_3)_2$ ($\rho_{DOL} = 2870$ kg/m^3). The post-dolomitisation porosity φ_{POST} is a function of the initial pre-dolomitisation porosity φ_o, the density of the calcite and dolomite, ρ_{LMST} and ρ_{DOL}, respectively, and the fraction of dolomite χ_{DOL}, and the molar masses of calcite M_{LMST} and dolomite M_{DOL} according to

$$\varphi_{POST} = \frac{2M_{LMST}[\chi_{DOL}\rho_{DOL} + (1-\chi_{DOL})\rho_{LMST}\varphi_o] - M_{DOL}[\chi_{DOL}\rho_{LMST}(1-\varphi_o)]}{2M_{LMST}[(1-\chi_{DOL})\rho_{LMST} + \chi_{DOL}\rho_{DOL}]}, \quad (8)$$

which, together with other equations in this section, is derived in Appendix A.

The post-depositional porosity depends upon both molar mass mixing and density mixing because the calculation of porosity change must be carried out on the same volume of rock, to which the result is normalised by making the porosity calculation. The value of 2 arises from the number of calcite molecules needed to produce one of dolomite in the chemical equilibrium between calcite and dolomite.

$$2CaCO_3 + Mg^{2+} = CaMg(CO_3)_2 + Ca^{2+}. \quad (9)$$

Examination of Equation (8) shows that when setting $\chi_{DOL} = 0$ (no dolomitisation) gives $\varphi_i = \varphi_o$, and setting $\chi_{DOL} = 1$ (full dolomitisation) results in

$$\varphi_{POST} = 1 - \frac{M_{DOL}}{2M_{LMST}}\frac{\rho_{LMST}}{\rho_{DOL}}(1-\varphi_o). \quad (10)$$

Full dolomitisation results in a porosity that is controlled by the ratio of the molar masses in Equation (9), i.e., $M_{DOL}/2M_{LMST}$ and the ratio of the densities ρ_{LMST}/ρ_{DOL}. As both of these are <1, their product is also <1 and hence $\varphi_{POST} > \varphi_o$.

Fig. 12 shows the post-dolomitisation porosity as a function of the degree of dolomitisation for limestones of 8 different initial porosities, ranging from 1% to 30%, together with the percentage increase of porosity that this represents.

If, for example, one takes a limestone with and initial porosity 20% (i.e., 0.2) and subjects it to a 40% degree of dolomitisation (blue line), there is an approximately 21.54% increase in porosity giving a final porosity of 24.3%. Fig. 12b shows that the effect of dolomitisation is greater for limestones with low initial porosities, with a limestone with an initial porosity of 5% more than doubling its porosity to 10.12% (a 102.34% increase) in porosity when subjected to a 40% dolomitisation.

Reference to the poroperm cross-plot shown in the poroperm diagram shown previously (Fig. 5) indicates the likely change in permeability associated with these changes in porosity. In the first case the increase in porosity from 20% to 24.3% would not result in any significant increase in permeability, whereas an increase from 5% to 10.12% would result in an order of magnitude increase of the permeability. Consequently, the same degree of dolomitisation can have very different effects on the transport properties of the rock, depending on the initial characteristics of the rock.

Fig. 13 shows post-dolomitisation porosity as a function of pre-dolomitisation porosity by implementing Equation (8) for 11 degrees of fractional dolomitisation from no dolomitisation to full dolomitisation. The two red dashed lines represent the 1:1 line for no dolomitisation but arbitrarily shifted in the *y*-direction, in order that the changes in the gradients of the parametric curves can be seen more easily. These curves show that the increase in porosity concomitant upon dolomitisation is less for rocks with initially higher porosities. Porosity, during deformation is a progressive process, with the initial porosity at any given instant being the final porosity resulting from the last phase of dolomitisation. Consequently, the interpretation of porosity increases due to dolomitisation from Figs. 12 and 13 need to be done with care. Take for example a limestone with a 5% porosity (solid black symbol) that is gradually submitted to dolomitisation until it is full dolomitised. The porosity pathway will not take the pathway shown by the dashed black arrow because the pre-dolomitisation porosity varies during the dolomitisation process. Rather, the porosity pathway during dolomitisation might be expected to follow the solid black arrow in Fig. 13, until a final porosity is reached (open symbol).

Equation (8) can be inverted to allow the calculation of the initial

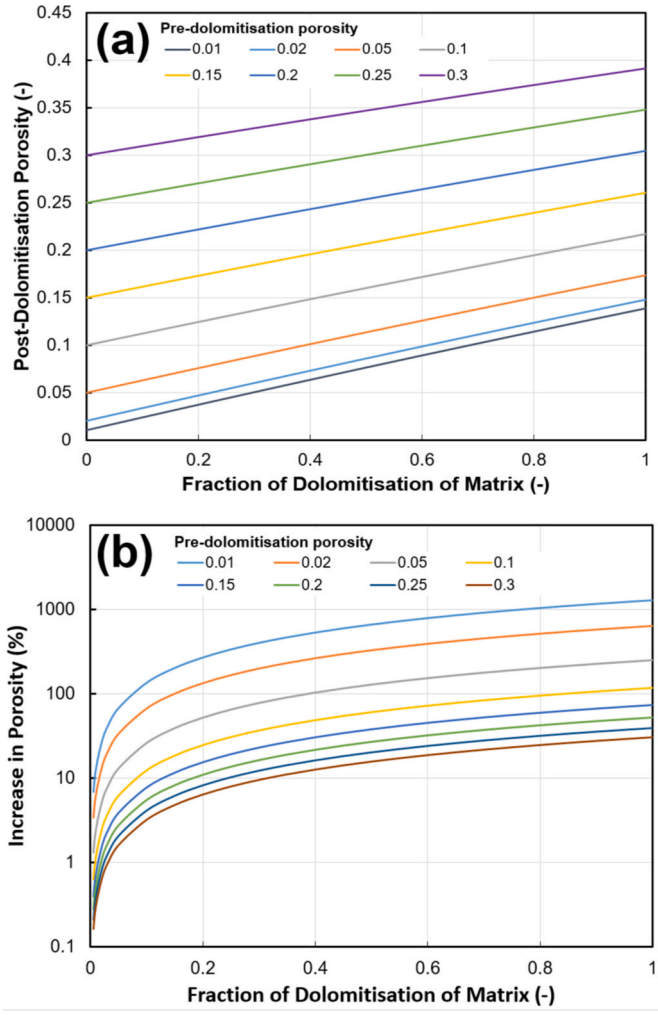

Fig. 12. (a) The post-dolomitisation porosity as a function of the degree of dolomitisation expressed as a fraction of the matrix for 8 rocks with different initial porosities, ranging from 1% porosity to 30% porosity. (b) The associated percentage increase in porosity as a function of fractional dolomitisation for the same samples.

porosity of a rock whose post-dolomitisation porosity is known if the composition is also known. The equation, which is derived in Appendix A, is

$$\varphi_o = \frac{2M_{LMST}[(1-\chi_{DOL})\rho_{LMST}\varphi_{POST} - \chi_{DOL}\rho_{DOL}(1-\varphi_{POST})] + M_{DOL}\chi_{DOL}\rho_{LMST}}{2M_{LMST}(1-\chi_{DOL})\rho_{LMST} + M_{DOL}\chi_{DOL}\rho_{LMST}}. \quad (11)$$

Once again, setting $\chi_{DOL} = 0$ (no dolomitisation), results in Equation (10) giving $\varphi_o = \varphi_{POST}$, and setting $\chi_{DOL} = 1$ (full dolomitisation) results in

$$\varphi_o = 1 - \frac{2M_{LMST}}{M_{DOL}}\frac{\rho_{DOL}}{\rho_{LMST}}(1-\varphi_{POST}). \quad (12)$$

This equation can be rearranged to produce Equation (10) and is likewise controlled by the ratios of the molar masses and densities of the calcite and dolomite.

Fig. 14 shows Equation (11), where each curve represents the post-dolomitisation porosity that arises from a given pre-dolomitisation porosity and degree of dolomitisation. It can be used to obtain the pre-dolomitisation porosity for a rock whose degree of dolomitisation and current porosity is known. This is done by interpolating between the curves for the current porosity and read the *y*-axis value for the point on the interpolated curve at the given degree of dolomitisation.

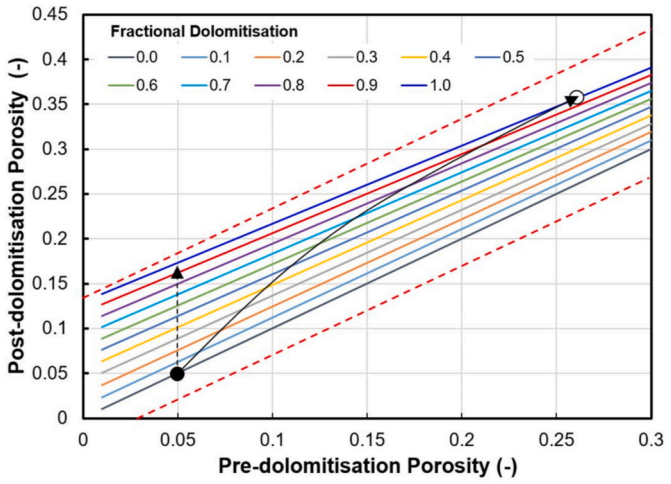

Fig. 13. Post-dolomitisation porosity as a function of pre-dolomitisation porosity from Equation (8) for 11 degrees of fractional dolomitisation from no dolomitisation to full dolomitisation. The two red dashed lines represent the 1:1 line for no dolomitisation but arbitrarily shifted in the *y*-direction and act as eye-guides. The symbols and black arrows show examples of a porosity pathway followed (solid arrow) and not followed (dashed arrow) during dolomitisation. (For interpretation of the references to colour in this figure legend, the reader is referred to the Web version of this article.)

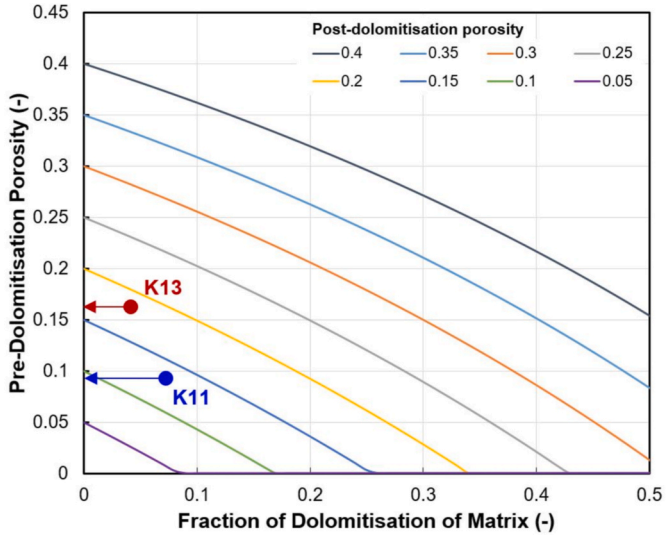

Fig. 14. Pre-dolomitisation porosity as a function of fraction of dolomitisation from Equation (11) for various degrees of post-dolomitisation porosity. Samples K11 and K13 are plotted using the known values of χ_{Dol} and interpolating between the curves for pre-dolomitisation porosity to calculate the pre-dolomitisation porosity (*y*-axis).

We can apply Equation (11) to samples where we know both the post-dolomitisation porosity and dolomite fraction of the sample. Two such samples are K11 and K13, which have 7.41% and 4.5% dolomite, and post-dolomitisation porosities of 13.2% and 18.3%, respectively. The calculated pre-dolomitisation porosities are 9.19% and 16.04%, respectively, which correspond to increases of 4.01% and 2.26% of porosity as a result of dolomitisation. These two examples are plotted on Fig. 14.

Either (8) or (11) can be rearranged to provide an equation for calculating the fraction of dolomitisation χ_{DOL}

$$\chi_{DOL} = \frac{2M_{LMST}\rho_{LMST}(\varphi_{POST} - \varphi_o)}{2M_{LMST}[\rho_{DOL}(1-\varphi_{POST}) + \rho_{LMST}(1-\varphi_o)] - M_{DOL}\rho_{LMST}(1-\varphi_o)}. \quad (13)$$

The previous equations make the assumption that increasing degrees of dolomitisation only leads to greater and greater porosities. However, this is not the case. While small amounts of dolomitisation generally increases porosity, and that increase can be followed by using equations (4) and (5) further dolomitisation ultimately leads to the occlusion of some of the existing pores with dolomite. This so-called 'over-dolomitisation' process can lead to local decreases in porosity. However, mass-balance ensures that patches of porosity loss due to over-dolomitisation must be balanced by dolomite loss elsewhere, perhaps causing even greater porosities. The use of the equations outlined above may consequently be only valid for a given, currently unknown, range of dolomitisation extent, or in given particular local areas.

Nevertheless, equations (4) and (5) provide the researcher with new methods for calculating either the degree of dolomitisation, pre-dolomitisation porosity or post-dolomitisation porosity if the other two parameters are known. Diagenesis is often treated qualitatively in the scientific literature. We hope that these equations will be the first step in treating the discussion of dolomitisation more quantitatively, and to be able to further develop a more quantitative treatment of the effects of diagenesis by viewing the effects of diagenesis through the examination of a wide range of rock petrophysical properties.

4.9. Fracturing

Fracturing can be considered to be (i) a pre-diagenetic process, providing fluids for dissolution, precipitation and dolomitisation access to the rocks, (ii) a diagenetic process, acting to significantly change the rock's properties by post-depositional mechanical change, or (iii) a post-diagenetic process, resulting from changes to the rock's mechanical properties concomitant upon process of diagenesis which have occurred (Becker et al., 2018; Rashid et al., 2020; Mohammed Sajed and Glover, 2020). Fracturing might occur due to Process (iii) associated with one phase of diagenesis, providing fractures which allow a further phase of diagenesis to occur.

In this work we have not presented data from fractured samples. However, fractured samples occur in the dataset we have been studying. These samples exhibit multiple orders of magnitude increases in permeability associated with little increase in porosity.

Efficient fluid flow through the fracture network also leads to low formation factors, high electrical connectednesses, low cementation exponents (approaching unity for pervasively fractured samples (Glover, 2015)) and low electrical tortuosities (Rashid et al., 2015a; 2015b; 2017). Calculations of permeability using the RGPZ model (Glover et al., 2006) shows that a rock with an initial porosity of 10% and an initial cementation exponent of $m = 2$, which is typical of a non-fractured sandstone, increases in permeability from 0.058 mD to 7.54 mD (over two orders of magnitude) if the cementation exponent is reduced to $m = 1.4$ by the development of fracturing.

Associated diagenesis is usually proximal to the induced fractures. However, the presence of fractures increases access of associated matrix to the effects of pervading fluids, and may lead to changes where none would be possible in the absence of the fractures.

5. Petrodiagenetic pathways

In the previous results and discussion sections we have shown that the petrophysical properties of a rock depend in a very complex manner on the way that the type, style and timing of diagenetic processes modify the microstructural parameters that define the rock and act upon the measured petrophysical properties via a set of phase fractions and connectednesses. These relationships are commonly counterintuitive. Here we describe a method for plotting the changes in the porosity and permeability concomitant upon the operation of concurrent and penecontemporaneous diagenetic processes. Here we consider porosity and permeability, but any two measureable parameters may be used. An obvious alternative choice would be permeability and electrical connectedness.

Mohammed Sajed and Glover (2020) and Mohammed Sajed et al. (2021) examined the diagenetic processes occurring in tight carbonates with a view towards understanding their effect on the poroperm properties, and hence classifying their reservoir qualities, while Al-Khalifah et al. (2020) have examined the effect of diagenesis on permeability prediction using neural networks and genetic algorithms. Towards the end of the Al-Khalifah et al. (2020) paper a schematic characterisation for the expected pathway through porosity-permeability space (φ-k space) that would be expected to result from different diagenetic processes was introduced. Here we develop this idea further and fully describe the final model, naming the pathways that develop in φ-k space as petrodiagenetic pathways.

Part (a) of Fig. 15 shows the main aspects of the model. A given rock is characterised by a porosity and permeability that defines a position on a poroperm plot. The operation of a diagenetic process on the rock modifies the porosity and permeability in such a way that the rock plots at a different place on the poroperm plot after the diagenetic process has been completed.

Different diagenetic processes have different relative effects upon porosity and permeability. For example, fracturing increases the permeability greatly for a small augmentation of porosity, while dolomitisation increases porosity as well as permeability. Compaction tends to reduce both porosity and permeability across the whole of the pore microstructure whereas precipitation/cementation tends to block pore throats more locally and more efficiently, leading to greater permeability reductions per loss of unit porosity. Hence, the arrows in Fig. 15a represent the characteristic direction in φ-k space associated with a particular diagenetic process. The lengths of the arrows is related to the degree of development or expression of the diagenetic process. Consequently, the movement in φ-k space is related to the type and degree of diagenetic process.

We propose that pathways of successive diagenetic process can be plotted on a poroperm plot to produce what we will call a Petrodiagenetic Pathway, an example of which is shown in Part (b) of Fig. 15. These represent pathways that may be followed by the timing of diagenetic processes in porosity-permeability space, and may be compared to underlying poroperm data, if available.

In the example given in Fig. 15b, a limestone formation initially has a pore microstructure such that it plots at Point A on the poroperm diagram. Point A is associated with a given cementation exponent (here $m = 2$) and characteristic grain size (here $d_{grain} = 30$ μm) which is described by the RGPZ contour passing through it. Subsequently, the formation undergoes dolomitisation, as shown by the orange arrow. The result of the dolomitisation is that the porosity of the rock increases, which leads to a greater connectivity of the pores and a higher permeability. Dolomite is more brittle than the initial limestone. Hence, dolomitisation makes the formation susceptible to fracturing, the result of which is shown by the blue arrow. Such fracturing increases the porosity of the rock by only a small amount, but the resulting increase in pore network connectivity is large and leads to a substantial increase in permeability. The fracturing is followed by compaction, shown by the grey arrow, leading to a smaller porosity and permeability than fracturing with no compaction would have achieved. The open fractures that were formed then allow mineral-rich fluids to enter the rock and for precipitation/cementation to occur, both in the fractures and in the proximal pore matrix, as shown by the red arrow. The cementation reduces both the porosity by replacing open pores and fractures with mineralisation, but also reduces permeability by blocking pore-throats, and hence reducing the number of pathways for fluid flow. The resulting formation has a porosity and permeability represented by Point B, which, in this example, is lower in porosity than the initial state but has a

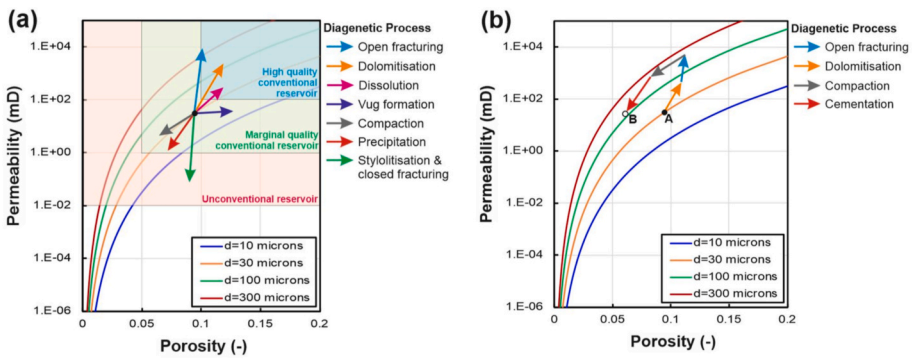

Fig. 15. (a) The effect of different diagenetic processes on the poroperm expression in tight carbonate rocks (modified after Al-Khalifah et al., 2020). Here, the contour lines represent the results of the modified carbonate RGPZ model for grain sizes (Rashid et al., 2015b). The arrows for different diagenetic processes refer to an arbitrary point on one of the curves, but equally well apply to any point on any of the curves (after Al-Khalifah et al., 2020). (b) The result of successive diagenetic processes on the plot as an petrodiagenetic pathway as described in the text.

similar permeability. It also lies on an RGPZ contour representing a higher characteristic grain size than initially, which is due primarily to the dolomitisation.

In this model concurrent processes can also be represented by the vector sum of two arrows, such that the net effect of, say, dolomitisation and vug formation is approximately the same as dissolution. In the example shown in Fig. 15b it can be noted that the pathway taken in the order dolomitisation/fracturing/compaction/cementation leads to the same end-point as dolomitisation/compaction/fracturing/cementation. Mathematically this means that concurrent processes can be represented on such a pathway as consecutive processes. Indeed, the whole pathway is a simple vector sum of the different diagenetic vectors. However, this mathematical relationship does not imply that the same end-point will be reached if the diagenetic processes actually occurred in a different order because the lengths of each of the vectors would be different as a result of the degree of expression of the diagenetic process being different. Taking the example once again, the degree of fracturing depended upon the previous dolomitisation. The degree of compaction depended upon the fracturing and the cementation also depended on the fracturing and the degree to which compaction may have partially closed those fractures. Hence, the history of the evolution of the rock is important in determining the petrodiagenetic pathway.

It should also be noted that (i) fluid flow is a vector quantity, (ii) formations generally exhibit some degree of anisotropy, and (iii) the process of fracturing is highly direction dependent, controlled as it is by the stress tensor. Consequently, a full expression of the rock should be a triad of poroperm figures for each of φ-k_x, φ-k_y, and φ-k_z, where the Cartesian coordinates x, y and z are northwards, westwards and vertically, respectively. Petrodiagenetic pathways will generally be different in each of these direction sensitive φ-k plots.

There are many interactions which may occur between petrophysical properties and diagenetic processes. Each will control the direction and length of the vectors directing the petrodiagenetic pathway. For example, dissolution can increase the porosity, but have little effect on permeability, while other processes, such as fracturing can affect permeability much more than porosity. This distinction is easy to incorporate in a petrodiagenetic pathway as each will influence the direction of the relevant petrodiagenetic vector. In another example, dolomitisation may increase porosity, but over-dolomitisation can result in subsequent decreases in porosity. In any case, the increase in the mass fraction of dolomite will enhance the resistance of the rock to compaction, protecting it from porosity reduction, while making fracturing more likely in order to reduce local stresses. The extent to which the interaction between different types of diagenesis influence the petrodiagenetic pathway is clearly a subject for further study.

As indicated at the start of this section, we have developed the idea of petrodiagenetic pathways for φ-k space (i.e., poroperm). This is useful because it allies porosity, which is the phase fraction for the pore space, with hydraulic permeability, which is a property highly dependent on the connectedness of the pore space. Both are also well-understood and commercially important. However, the concept of petrodiagenetic pathways can equally be applied to other spaces. One alternative is φ-G_{pore} space, which would be useful if permeability measurements were not available, but electrical measurements were. Another possibility would be to use χ_{matrix}-G_{matrix} space for considering elastic wave or thermal properties (calculating both using equations (6) and (7).

The definition of petrodiagenetic pathways as a tool for studying diagenesis is only the first step in the development of an approach to quantitative diagenesis. For such a technique to be applicable to any particular formation, it requires information about the type, degree and timings of different episodes of diagenesis. This information is potentially available from the study of the mineralogy and microstructure of the formation (e.g., Hollis and Al Hajri, 2022; Mohammed-Sajed and Glover, 2022), from studies of the evolution of geochemical signatures, from the use of cathodolumiescence and also fluid inclusion studies (e.g., Chen et al., 2021; Burley et al., 1989), as well as a number of other combined approaches (Elias Bahnan et al., 2021). For a given formation, such studies may be demanding of time and research resources. However, now there exists an analytic framework in which the various diagenetic changes can be represented quantitatively.

6. Conclusions

Conventionally, diagenetic processes in carbonate rocks and their ultimate effect on the physical properties of rocks as well as their reservoir quality have been studied qualitatively through classification schemes based on morphological observations. Petrophysics offers new quantitative approaches for measuring rock properties that have been modified by diagenetic processes.

In this paper we have attempted to use a large dataset of petrophysical measurements to explore the effects of diagenesis in a quantitative manner. Our approach has been to develop a new theoretical framework linking diagenetic processes to the petrophysically measureable physical properties of the rock. This framework has been used to explain expected and newly-observed counter-intuitive relationships, to develop new approaches for calculating pre- and post-dolomitisation porosities, to suggest novel ways of predicting cementation exponents, and to introduce a new 'Petrodiagenetic Pathways' method for tracking the effects of diagenetic process by using petrodiagenetic pathways.

These advances represent the start to the process of putting the study of those diagenetic process which modify rock textures in subtle and inter-linked ways on a more theoretical basis that can be used to predict the effects of different degrees of diagenesis for the purposes of understanding the diagenetic history of rocks as well as predicting their quality as a reservoir.

We recommend that all future studies of carbonate diagenesis take advantages of the numerous and high quality petrophysical measurements that are now available, and interpret those data using the emerging quantitative analysis methods, in parallel with more conventional observational and classification methods.

Declaration of competing interest

The authors declare that they have no known competing financial interests or personal relationships that could have appeared to influence the work reported in this paper.

Acknowledgements

This study was funded by the Ministry of Higher Education of the Iraqi Kurdistan Region government as a part of the Human Capacity Development Programme (HCDP). We express our gratitude to the Ministry of Natural Resources of Kurdistan Region and the Ministry of Oil of the Iraqi government for providing the project data. Finally, our special thanks go to Richard Collier and the Wolfson Multiphase Flow Laboratory's team at Leeds University; Quentin Fisher, Carlos Grattoni, Phil Guise and Samuel Allshorn.

Appendix A. Derivation of Dolomitisation Equations

A given mass of rock contains an initial porosity φ_o and hence a matrix fraction (1- φ_o).

Assuming that the rock is completely composed of calcite (i.e., pure limestone), the mass of the rock matrix is

$$M = \rho_{LMST} V(1-\varphi_o) = NM_{LMST}, \tag{A.1}$$

where, M is the mass of the rock matrix, ρ_{LMST} is the density of the calcite, V is the rock bulk volume, φ_o is the initial porosity of the rock, M_{LMST} is the molar mass of calcite, and N is the number of moles of calcite.

Rearranging (A.1) for volume gives

$$V = \frac{NM_{LMST}}{\rho_{LMST}(1-\varphi_o)} \tag{A.2}$$

Assume that there is a net input of Mg^{2+} and a net outflow of Ca^{2+} through the porosity such that there is a degree of dolomitisation according to the equation

$$2CaCO_3 + Mg^{2+} = CaMg(CO_3)_2 + Ca^{2+}. \tag{A.3}$$

In this equation, 2 mol of calcite react to produce 1 mol of dolomite. Consequently, (A.2) must be rewritten as

$$V = \frac{2NM_{LMST}}{\rho_{LMST}(1-\varphi_o)}, \tag{A.4}$$

in order to balance (A.3) and hence to conserve the volume of the sample as calcite is dolomitised.

Now consider dolomitisation which results in the matrix evolving such that the dolomite phase fraction changes from 0 to χ_{DOL}, and the calcite phase changes from 1 to (1-χ_{DOL}). Repeating the procedure leading to (A.1) by balancing the masses, we can write

$$\rho_{LMST}(1-\chi_{DOL})V(1-\varphi_{POST}) + \rho_{DOL}\chi_{DOL}V(1-\varphi_{POST}) = N[2M_{LMST}(1-\chi_{DOL}) + M_{DOL}\chi_{DOL}], \tag{A.5}$$

where the porosity after dolomitisation is φ_{POST}.

Substituting (A.4) in (A.5) to eliminate V also eliminates N

$$\frac{2M_{LMST}\,(1-\chi_{DOL})\,\rho_{LMST}\,(1-\varphi_{POST})}{\rho_{LMST}(1-\varphi_o)} + \frac{2M_{LMST}\,\chi_{DOL}\,\rho_{DOL}\,(1-\varphi_{POST})}{\rho_{LMST}(1-\varphi_o)} = 2M_{LMST}(1-\chi_{DOL}) + M_{DOL}\chi_{DOL}, \tag{A.6}$$

which, when simplified, gives Equation (A.7)

$$\varphi_{POST} = \frac{2M_{LMST}[\chi_{DOL}\rho_{DOL} + (1-\chi_{DOL})\rho_{LMST}\varphi_o] - M_{DOL}[\chi_{DOL}\rho_{LMST}(1-\varphi_o)]}{2M_{LMST}[(1-\chi_{DOL})\rho_{LMST} + \chi_{DOL}\rho_{DOL}]}, \tag{A.7}$$

Examination of Equation (A.7) shows that:

- when setting $\chi_{DOL} = 0$ (no dolomitisation) (A.7) gives $\varphi_{POST} = \varphi_o$.
- when setting $\chi_{DOL} = 1$ (full dolomitisation) (A.7) gives

$$\varphi_{POST} = 1 - \frac{M_{DOL}}{2M_{LMST}}\frac{\rho_{LMST}}{\rho_{DOL}}(1-\varphi_o). \tag{A.8}$$

Equation (A.7) can be rearranged to provide an equation for calculating

$$\varphi_o = \frac{2M_{LMST}[(1-\chi_{DOL})\rho_{LMST}\varphi_{POST} - \chi_{DOL}\rho_{DOL}(1-\varphi_{POST})] + M_{DOL}\chi_{DOL}\rho_{LMST}}{2M_{LMST}(1-\chi_{DOL})\rho_{LMST} + M_{DOL}\chi_{DOL}\rho_{LMST}}. \tag{A.9}$$

Examination of Equation (A.9) shows that:

- when setting $\chi_{DOL} = 0$ (no dolomitisation) (A.9) gives $\varphi_o = \varphi_{POST}$
- when setting $\chi_{DOL} = 1$ (full dolomitisation) (A.9) gives

$$\varphi_o = 1 - \frac{2M_{LMST}}{M_{DOL}}\frac{\rho_{DOL}}{\rho_{LMST}}(1-\varphi_{POST}). \tag{A.10}$$

which can be rearranged to give (A.8).

Either (A.7) or (A.9) can be rearranged to provide an equation for calculating the fraction of dolomitisation χ_{DOL}

$$\chi_{DOL} = \frac{2M_{LMST}\rho_{LMST}(\varphi_{POST} - \varphi_o)}{2M_{LMST}[\rho_{DOL}(1-\varphi_{POST}) + \rho_{LMST}(1-\varphi_o)] - M_{DOL}\rho_{LMST}(1-\varphi_o)}. \quad (A.11)$$

References

Adam, A., Swennen, R., Abdulghania, W., Abdlmutalib, A., Hariria, M., Abdulraheem, A., 2018. Reservoir heterogeneity and quality of Khuff carbonates in outcrops of central Saudi Arabia. Mar. Petrol. Geol. 89, 721–751.

Akbar, M., Steckhan, J., Tamimi, M., Zhang, T., Saner, S., 2008. Estimating cementation factor (m) for carbonates using borehole images and logs. Paper SPE-117786-MS. In: Abu Dhabi International Petroleum Exhibition and Conference. Society of Petroleum Engineers, Abu Dhabi, United Arab Emirates, 3-6 November 2008.

Aldega, L., Bigi, S., Carminati, E., Trippetta, F., Corrado, S., Kavoosi, M.A., 2018. The Zagros fold-and-thrust belt in the Fars province (Iran): II. Thermal evolution. Mar. Petrol. Geol. 93, 376–390.

Alsharhan, A.S., Sadd, J.L., 2000. Stylolites in Lower Cretaceous Carbonate Reservoirs, vol. 69. U.A.E. SPE special publication, pp. 185–207.

Al Khalifah, H., Glover, P.W.J., Lorinczi, P., 2020. Permeability prediction and diagenesis in tight carbonates using machine learning techniques. Mar. Petrol. Geol. 112, 104096.

Al-Qayim, B., Othman, D., 2012. Reservoir characterization of an intra-orogenic carbonates platform: pila Spi Formation. In: Taq Taq Oil Field, vol. 370. Geological Society, London, Special Publications, Kurdistan, Iraq, pp. 139–168.

Al-Qayim, B., Rashid, F., 2012. Reservoir characteristics of the albian upper qamchuqa formation carbonates, Taq Taq oilfield, kurdistan, Iraq. J. Petrol. Geol. 35, 317–341.

Anselmetti, F.S., Von Salis, G.A., Cunningham, K.J., Eberli, G.P., 1997. Acoustic properties of Neogene carbonates and siliciclastics from the subsurface of the Florida Keys: implications for seismic reflectivity. Mar. Geol. 144, 9–31.

Anselmetti, F.S., Eberli, G.P., 1993. Controls on sonic velocity in carbonates. Pure Appl. Geophys. PAGEOPH 141, 287–323.

Anselmetti, F.S., Eberli, G.P., 1997. Sonic velocity in carbonate sediments and rocks. Carbonate Seismol 53–74. https://doi.org/10.1190/1.9781560802099.ch4.

Archie, G.E., 1942. The electrical resistivity log as an aid in determining some reservoir characteristics. Paper SPE-942054-G, Society of Petroleum Engineers. Transactions of the AIME 146 (1), 54–62.

Barros-Galvis, N.E., 2018. Geomechanics, Fluid Dynamics and Well Testing, Applied to Naturally Fractured Carbonate Reservoirs: Extreme Naturally Fractured Reservoirs. Springer.

Becker, I., Koehrer, B., Waldvogel, M., Jelinek, W., Hilgers, C., 2018. Comparing fracture statistics from outcrop and reservoir data using conventional manual and t-LiDAR derived scanlines in Ca2 carbonates from the Southern Permian Basin, Germany. Mar. Petrol. Geol. 95, 228–245.

Bigi, S., Carminati, E., Aldega, L., Trippetta, F., Kavoosi, M.A., 2018. Zagros fold and thrust belt in the Fars province (Iran) I: control of thickness/rheology of sediments and pre-thrusting tectonics on structural style and shortening. Mar. Petrol. Geol. 91, 211–224.

Borai, A.M., 1987. A new correlation for cementation factor in low- porosity carbonates. Paper SPE-14401-PA, Society of Petroleum Engineers. SPE Form. Eval. 2 (4), 495–499.

Burley, S.D., Mullis, J., Matter, A., 1989. Timing diagenesis in the Tartan Reservoir (UK North Sea): constraints from combined cathodoluminescence microscopy and fluid inclusion studies. Mar. Petrol. Geol. 6 (2), 98–104. IN1-IN4,105-120.

Cai, J., Wei, W., Hu, X., Wood, D.A., 2017. Electrical conductivity models in saturated porous media: a review. Earth Sci. Rev. 171, 419–433.

Carpenter, P.J., Ding, A.Z., Cheng, L.R., Liu, P., Chu, F., 2009. Apparent formation factor for Leachate-Saturated waste and sediments: examples from the USA and China. J. Earth Sci. 20 (3), 606–617.

Chen, L.Q., Zou, C.C., Wang, Z.H., Liu, H., Yao, S., Chen, D., 2009. Logging evaluation method of low resistivity reservoir—a case study of well block DX12 in Junggar basin. J. Earth Sci. 20 (6), 1003–1011.

Chen, P., Fu, M., Deng, H., Xu, W., Wu, D., He, P., Guo, H., 2021. The diagenetic alteration of the carbonate rocks from the Permian Qixia formation as response to two periods of hydrothermal fluids charging in the central uplift of Sichuan basin, SW China. Minerals 11 (11).

Choquette, P.W., Pray, L.C., 1970. Geological nomenclature and classification of porosity in sedimentary carbonates. AAPG Bulletin 54, 207–250.

Davies, G.R., Smith, J., 2006. Structurally controlled hydrothermal dolomite reservoir facies: an overview. AAPG (Am. Assoc. Pet. Geol.) Bull. 90 (11), 1641–1690.

Dix, G.R., Mullins, H.T., 1987. Shallow, subsurface growth and burial alteration of Middle Devonian calcite concretions. J. Sediment. Res. 57 (1), 140–152.

Elias Bahnan, A., Pironon, J., Carpentier, C., Barré, G., Gaucher, E.C., 2021. The diagenetic history of the giant Lacq gas field, witness to the apto-albian rifting and the Pyrenean orogeny, revealed by fluid and basin modeling. Mar. Petrol. Geol. 133.

Garum, M., Glover, P.W.J., Lorinczi, P., Micklethwaite, S., Hassanpour, A., 2021a. Integration of multiscale imaging of nanoscale pore microstructures in gas shales. Energy Fuel. 35 (13), 10721–10732.

Garum, M., Glover, P.W.J., Lorinczi, P., Scott, G., Hassanpour, A., 2021b. Ultrahigh-resolution 3D imaging for quantifying the pore nanostructure of shale and predicting gas transport. Energy Fuel. 35 (1), 702–717.

Glover, P.W.J., 2009. What is the cementation exponent? A new interpretation. Lead. Edge 28 (1), 82–85.

Glover, P.W.J., 2010. A generalized Archie's law for n-phases. Geophysics 75, E247–E265.

Glover, P.W.J., 2015. Geophysical properties of the near surface earth: electrical properties. In: Treatise on Geophysics, second ed., pp. 89–137.

Glover, P.W.J., 2016. Archie's law - a reappraisal. Solid Earth 7, 1157–1169.

Glover, P.W.J., 2017. A new theoretical interpretation of Archie's saturation exponent. Solid Earth 8, 805–816.

Glover, P.W.J., Hole, M., Pous, J., 2000. A modified Archie's law for two conducting phases. Earth Planet Sci. Lett. 180 (3), 369–383.

Glover, P.W.J., Zadjali, I.I., Frew, K.A., 2006. Permeability prediction from MICP and NMR data using an electrokinetic approach. Geophysics 71 (4), 49–60.

Glover, P.W.J., Walker, E., 2009. Grain-size to effective pore-size transformation derived from electrokinetic theory. Geophysics 74 (1), 17–29.

Glover, P.W.J., Déry, N., 2010. Streaming potential coupling coefficient of quartz glass bead packs: dependence on grain diameter, pore size, and pore throat radius. Geophysics 75 (6), F225–F241.

Gomez-Rivas, E., Martín-Martín, J.D., Bons, P.D., Koehn, D., 2015. Can stylolite networks control the geometry of hydrothermal alterations? Geotect. Res. 97, 34–36.

Heap, M.J., Baud, P., Reuschlé, T., Meredith, P.G., 2014. Stylolites in limestones: barriers to fluid flow? Geology 42, 51–54.

Hesse, R., Shah, J., Islam, S., 2004. Physical and chemical growth conditions of Ordovician organogenic deep-water dolomite concretions: implications for the δ18O of Early Palaeozoic sea water. Sedimentology 51, 601–625.

Hollis, C., 2011. Diagenetic on controls reservoir properties of carbonate successions with in the Albian–Turonian of the Arabian Plate. Petrol. Geosci. 17, 223–241.

Hollis, C., Lawrence, D.A., Perière, M.D., Al Darmaki, F., 2017. Controls on porosity preservation within a Jurassic oolitic reservoir complex. UAE. Marine and Petroleum Geology 88, 888–906.

Hollis, C., Vahrenkamp, V., Tull, S., Mookerjee, A., Taberner, C., Huang, Y., 2010. Pore system characterisation in heterogeneous carbonates: an alternative approach to widely-used rock-typing methodologies. Mar. Petrol. Geol. 27, 772–793.

Hollis, C., Al Hajri, A., 2022. Post-compactional porosity in a hydrocarbon-bearing carbonate succession: potential timing and processes controlling porosity creation in the Aptian Shuaiba Formation, Oman. Sediment. Geol. 428.

Höltzel, A., Tallarek, U., 2007. Ionic conductance of nanopores in microscale analysis systems: where microfluidics meets nanofluidics. J. Separ. Sci. 30 (10), 1398–1419.

Hussein, D.O., Collier, R., Lawrence, J.A., Rashid, F., Glover, P.W.J., Lorinczi, P., Baban, D.H., 2017. Stratigraphic correlation and paleoenvironmental analysis of the hydrocarbon bearing Early Miocene Euprates and Jeribe formations in the Zagros Folded-Thrust belt. Arabian Journal of Geoscienece 10 (24), 543.

Hussein, D., Lawrence, J., Rashid, F., Glover, P., Lorinczi, P., 2018. Developing pore size distribution models in heterogeneous carbonates using especially nuclear magnetic resonance. In: Engineering in Chalk: Proceedings of the Chalk 2018 Conference. ICE Publishing, pp. 529–534.

Jafarian, A., Fallah-Bagtash, R., Mattern, F., Heubeck, C., 2017. Reservoir quality along a homoclinal carbonate ramp deposit: the permian upper dalan formation, south pars field, Persian gulf basin. Mar. Petrol. Geol. 88, 587–604.

Jones, S.C., 1997. A technique for faster pulse-decay permeability measurements in tight rocks. SPE Form. Eval. 12 (01), 19–25. Paper Number: SPE-28450-PA.

Lawrence, M.J.F., 1991. Early diagenetic dolomite concretions in the late cretaceous herring formation, eastern marlborough, New Zealand. Sediment. Geol. 75 (1–2), 125–140.

Liu, H., Tian, Z., Liu, B., Guo, R., Yang, D., Deng, Y., Yu, Y., Shi, K., 2018. Pore types, origins and control on reservoir heterogeneity of carbonate rocks in Middle Cretaceous Mishrif Formation of the West Qurna oilfield, Iraq. J. Petrol. Sci. Eng. 171, 1338–1349.

Liu, H., Shi, K., Liu, B., Song, X., Guo, R., Li, Y., Wang, G., Wang, H., Shen, Y., 2019. Characterization and identification of bioturbation-associated high permeability zones in carbonate reservoirs of Upper Cretaceous Khasib Formation, AD oilfield, central Mesopotamian Basin, Iraq. Mar. Petrol. Geol. 110, 747–767.

Liu, Z., Zhang, Y., Song, G., Li, S., Long, G., Zhao, J., Zhu, C., Wang, Y., Gong, Q., Xia, Z., 2021. Mixed carbonate rocks lithofacies features and reservoirs controlling mechanisms in a saline lacustrine basin in Yingxi area, Qaidam Basin, NW China. Petrol. Explor. Dev. 48 (1), 80–94.

Lucia, F.J., 1995. Rock-fabrics/Petrophysical classification of carbonate pore space for reservoir characterization. Am. Assoc. Petrol. Geol. 79 (1995), 1275–1300.

Luo, P., Machel, H.G., 1995. Pore size and pore throat types in a heterogeneous dolostone reservoir, Devonian Grosmont Formation, Western Canada Sedimentary Basin. AAPG (Am. Assoc. Pet. Geol.) Bull. 79 (11), 1698–1720.

Luczaj, J.A., Harrison III, W.B., Williams, N.S., 2006. Fractured hydrothermal dolomite reservoirs in the devonian dundee formation of the central Michigan basin. AAPG (Am. Assoc. Pet. Geol.) Bull. 90 (11), 1787–1801.
Mohammed Sajed, O.K., Glover, P.W.J., 2020. Dolomitisation, cementation and reservoir quality in three Jurassic and Cretaceous carbonate reservoirs in north-western Iraq. Mar. Petrol. Geol. 115.
Mohammed Sajed, O.K., Glover, P.W.J., Collier, R.E.L., 2021. Reservoir quality estimation using a new ternary diagram approach applied to carbonate formations in north-western Iraq. J. Petrol. Sci. Eng. 196.
Mohammed-Sajed, O.K., Glover, P.W.J., 2022. Influence of anhydritisation on the reservoir quality of the Butmah Formation in north-western Iraq. Mar. Petrol. Geol. 135.
Martín-Martín, J.D., Gomez-Rivas, E., Bover-Arnal, T., Travé, A., Salas, R., Moreno-Bedmar, J.A., Tomás, S., Corbella, M., Teixell, A., Vergés, J., Stafford, S.L., 2013. The Upper Aptian to Lower Albian syn-rift carbonate succession of the southern Maestrat Basin (Spain): facies architecture and fault-controlled strata bound dolostones. Cretac. Res. 41, 217–236.
Mozley, P.S., Burns, S.J., 1993. Oxygen and carbon isotopic composition of marine carbonate concretions: an overview. J. Sediment. Res. 63 (1), 73–83.
Normi, R., Standen, E., 1997. Middle East well evaluation. Review. SPE18.
Ramakrishnan, T.S., Ramamoorthy, R., Fordham, E., Schwartz, L., Herron, M., Saito, N., Rabaute, A., 2001. A model-based interpretation methodology for evaluating carbonate reservoirs. In: Paper SPE-71704-MS, Society of Petroleum Engineers. Annual Technical Conference and Exhibition, 30 September-3 October (New Orleans).
Rashid, F., Glover, P.W.J., Lorinczi, P., Collier, R., Lawrence, J., 2015a. Porosity and permeability of tight carbonate reservoir rocks in the north of Iraq. J. Petrol. Sci. Eng. 133, 147–161.
Rashid, F., Glover, P.W.J., Lorinczi, P., Hussein, D., Collier, R., Lawrence, J., 2015b. Permeability prediction in tight carbonate rocks using capillary pressure measurements. Mar. Petrol. Geol. 68, 536–550.
Rashid, F., Glover, P.W.J., Lorinczi, P., Hussein, D., Collier, R., Lawrence, J., 2017. Microstructural controls on reservoir quality in tight oil carbonate reservoir rocks. J. Petrol. Sci. Eng. 156, 814–826.
Rashid, F., Hussein, D., Lawrence, J.A., Khanaqa, P., 2020. Characterization and impact on reservoir quality of fractures in the cretaceous Qamchuqa Formation, Zagros folded belt. Mar. Petrol. Geol. 113, 104117.
Schlumberger, 2009. Log Interpretation Charts. Sugarland, Texas, USA.
Schofield, N., Jerram, D.A., Holford, S., Archer, S., Mark, N., Hartley, A., Howell, J., Muirhead, D., Green, P., Hutton, D., Stevenson, C., 2018. Sills in sedimentary basins and petroleum systems. In: Breitkreuz, C., Rocchi, S. (Eds.), Physical Geology of Shallow Magmatic Systems. Springer, Berlin, Germany, pp. 273–294.
Serra, O., 1984. Fundamentals of Well-Log Interpretation 1, the Acquisition of Logging Data, vol. 15. Elsevier Science Publishers, Developments in Petroleum Science, p. 424. Part A.
Sissakian, V.K., Ibrahim, E.I., Ibrahim, F.A., Al-Ali, N.M., 2000. Geological Map of Iraq, Scale 1/1000000. State company of geological survey and mining, Baghdad, Iraq.
Tiab, D., Donaldson, E.C., 2004. Petrophysics: Theory and Practice of Measuring Reservoir Rock and Fluid Transport Properties. Gulf Professional Publishing, Oxford, UK, p. 889.
Walker, E., Glover, P.W.J., 2018. Measurements of the relationship between microstructure, pH, and the streaming and zeta potentials of sandstones. Transp. Porous Med. 121 (1), 183–206.
Wang, L., Mao, Z., Shi, Y., Tao, Q., Cheng, Y., Song, Y., 2014. A novel model of predicting Archie's cementation factor from nuclear magnetic resonance (NMR) logs in low permeability reservoirs. J. Earth Sci. 25 (1), 183–188.
Westphal, H., Surholt, I., Kiesl, C., Thern, H.F., Kruspe, T., 2005. NMR measurements in carbonate rocks: problems and an approach to a solution. Pure and Applied Geophysics PAGEOPH 162 (3), 549–570.
Zhu, X., Jin, Z., Liang, T., Yi, S., Wei, K., Gao, B., Shi, L., 2020. Depositional environment, diagenetic evolution, and their impact on the reservoir quality of the carboniferous KT-II carbonate in the Zhanazhol reservoir, Pre-Caspian Basin, Kazakhstan. Mar. Petrol. Geol. 117, 104411.